Grain-size dependent elastic-plastic deformation behaviour of inconel 625 alloy studied by in-situ neutron diffraction

GAO, Yubi, DING, Yutian, LI, Haifeng, DONG, Hongbiao, ZHANG, Ruiyao, LI, Jun and LUO, Quanshun <http://orcid.org/0000-0003-4102-2129>

Grain-size dependent elastic-plastic deformation behaviuor of Inconel 625 alloy studied by in-situ neutron diffraction

Yubi Gao[1,2,6], Yutian Ding[1,2,*], Haifeng Li[3], Hongbiao Dong[4,**], Ruiyao Zhang [5], Jun Li[4], Quanshun Luo[6]

1 State Key Laboratory of Advanced Processing and Recycling of Non-ferrous Metals, Lanzhou University of Technology, Lanzhou, Gansu, 730050, PR China
2 School of Materials Science and Engineering, Lanzhou University of Technology, Lanzhou, Gansu, 730050, PR China
3 State Key Laboratory of Nonferrous Metals and Processes, General Research Institute for Nonferrous Metals, Beijing, 100088, PR China
4 Department of Engineering, University of Leicester, Leicester, LE1 7RH, UK
5 Stress Map, Engineering & Innovation, Open University, Milton Keynes, MK7 6AA, UK
6 Materials and Engineering Research Institute, Sheffield Hallam University, Sheffield, S1 1WB, UK
*Corresponding author. State Key Laboratory of Advanced Processing and Recycling of Non-ferrous Metals, Lanzhou University of Technology, Lanzhou, Gansu, 730050, PR China.
** Corresponding author. Department of Engineering, University of Leicester, Leicester, LE1 7RH, UK.
E-mail addresses: dingyutian@126.com or dingyt@lut.edu.cn (Y. T. Ding), h.dong@le.ac.uk (H. B. Dong).

Abstract: The effect of grain size on elastic-plastic deformation and twinning behaviour of Inconel 625 alloy was studied. Alloy samples were investigated using compressive deformation analysis, in-situ neutron diffraction, electron backscatter diffraction, and transmission electron microscopy. The alloy was found to exhibit strong elastic and plastic anisotropy. Grain refining was found to have several advantages, including the increased grain-specific diffraction elastic moduli, improved compatibility and homogeneity of polycrystalline deformation, and enhanced yield strength at room temperature. Two strong preferred orientations were present in coarse-grained samples: the Copper orientation of {112}<111>, in deformed grains because of dislocation slip, and the Brass orientation of {110}<112>, in elongated grains owing to deformation twinning. The coarse-grained samples also showed large quantities of stacking faults, multiple-slip lines, and dislocations. In contrast, stacking faults were not observed in fine-grained samples, however, a dense presence of slip lines, dislocations, and dislocation pile-ups at grain boundaries were observed. The fine-grained samples exhibited a higher density of dislocations than the coarse-grained samples given the same applied load during compressive deformation. The deformation mechanisms of the coarse-grained alloy were dominated by dislocation slipping and the formation of stacking faults, while the deformation of the fine-grained alloy showed only dislocation slipping.
Keywords: Inconel 625 alloy, grain size, lattice strain, stacking fault, neutron diffraction

1. Introduction

Inconel 625 alloy is extensively used to manufacture ammonia cracker tubes in heavy water production plants owing to its excellent strength and creep resistance, good resistance to oxidation, corrosion, and hydrogen attack, excellent formability, and low hydrogen permeability at both ambient and elevated temperatures [1-2]. The severe service conditions of these tubes include high temperatures (600 °C), high pressures (14 MPa), and prolonged usage periods (~60,000 h), which lead to a significant increase in strength but loss of ductility and toughness that may subsequently result in premature failure [3-4]. Inconel 625 is a solid-solute-strengthened alloy created by adding Mo and Nb to a Ni-Cr-based matrix [5]. In addition, it can be further strengthened by forming precipitation phases through an aging treatment or while in service at high temperatures [6]. However, these traditional strengthening methods increase the strength properties at the expense of reduced ductility and toughness.

It has been increasingly reported in recent years that plainified materials could overcome the aforementioned paradox of strength and ductility by introducing stable interfaces, such as twin boundaries and low-angle boundaries, at various length scales with fewer or no alloying elements [7-9]. Twin boundaries with nanoscale spacings usually exhibit high thermal and mechanical stabilities to impede dislocation motion and enable dislocation slip accumulation, which result in improved strength and ductility [10-12]. For example, Lu et al. [13-14] found that introducing high-density nano-twin boundaries into pure copper metal could increase its strength by an order of magnitude while maintaining good tensile ductility and high electrical conductivity. It has been reported that twin boundaries with nanometre-scale spacings make a significant contribution to excellent strength and ductility in materials [15]. Yuan et al. [16-17] proposed a novel strategy for a Ni-Co-based superalloy designed using twinning structures, wherein micro-twins enhanced its tensile and creep strengths without degrading other mechanical properties, such as low cycle fatigue, crack growth rate, and hot workability. These breakthroughs imply new possibilities for improving both the strength and ductility of Inconel 625 alloy through the tailoring of twin boundaries.

Considering the behaviour of nanoscale twin boundaries in nickel alloys, early studies [18-19] reported that severe plastic deformation of Inconel 625 and 600 alloys led to the generation of high-density deformation nano-twins on {111} planes. For Inconel 625 alloy under certain deformation conditions, the formation of deformation twins was strongly influenced by stacking fault energy (SFE) and grain size [20-21]. The critical shear stress for twinning decreased with reduced SFE and increased grain size. These findings suggest that, materials with a low SFE and a large grain-size favour deformation twinning, especially at high-strain rates and/or at low temperatures. In addition, grain orientation was found to have a significant influence on deformation twinning [21,22]. However, detailed experimental results are still required to understand the effects of grain size and grain orientation on elastic and plastic deformation behaviour and, in particular, on twinning behaviour of Inconel 625 alloy. In this work, we investigate the effect of Inconel 625 alloy grain size on its elastic and plastic deformation behaviour at room temperature, with a particular attention paid to its twinning behaviour under compressive deformation. In-situ neutron diffraction was used to evaluate elastic and plastic deformation behaviour as a function of grain size. In addition, post-mortem analysis of the deformed microstructures was conducted using electron backscatter diffraction (EBSD) and transmission electron microscopy (TEM) to the validate neutron diffraction results. Finally, the contribution of grain size on twinning stress and yield strength has been discussed.

2. Materials and methods

2.1. Materials

Inconel 625 alloy, a nickel-based superalloy, was investigated; its chemical composition is presented in Table 1. The alloy was produced via a dual process of vacuum induction melting and electro-slag remelting. To obtain coarse-grained and fine-grained microstructures, different heat treatments were applied to the alloy. Rod specimens with a diameter and length of 12 mm and 32 mm, respectively, were subjected to a two-stage homogenisation heat treatment (1140 °C for 10 h then 1210 °C for 48 h) followed by air cooling to room temperature, as shown in Fig. 1a. This treatment resulted in an average grain size of 800 μm and a strong grain orientation. The specimens obtained at this condition are referred to hereafter as the coarse-grained samples. Following the aforementioned treatment, some of the homogenised rods were subjected to hot extrusion at 1170 °C with a speed of 100 mm/s and an extrusion ratio of 6.66 using a 50 MN

Table 1 Chemical composition of Inconel 625 alloy. (wt.%)

Ni	Cr	Mo	Nb	Fe	Ti	Al	C	P	S
Bal.	21.77	8.79	3.75	3.68	0.40	0.21	0.042	0.006	0.0006

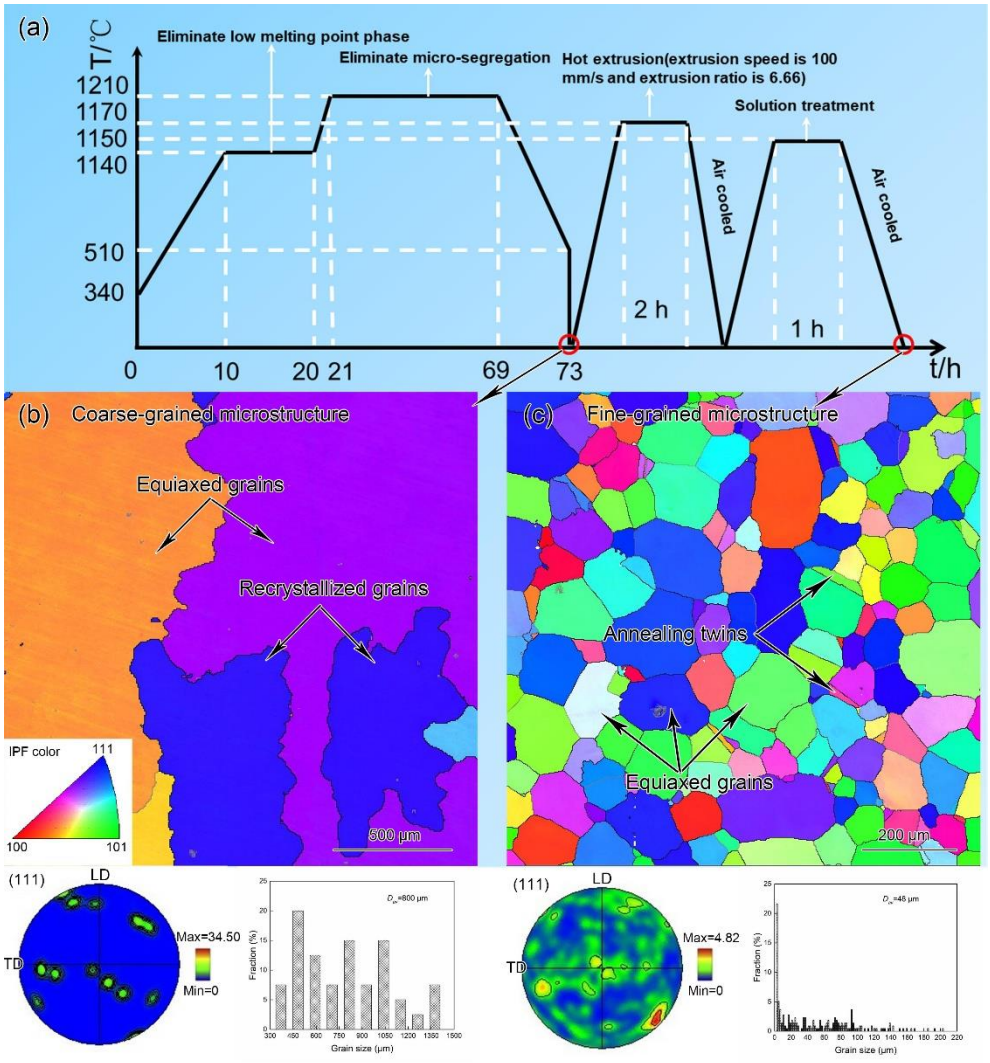

Fig.1 (a) Treatment steps involved in the generation of coarse-grained and fine-grained microstructures, and EBSD of (b) coarse-grained and (c) fine-grained microstructure.

horizontal extrusion press. Samples then underwent a solution treatment at 1150 °C for 1 h and air cooling to room temperature, as shown in Fig. 1a. These treatments resulted in an average grain size of 48 μm with a weak grain orientation; these samples are referred to as the fine-grained samples. Figs. 1b and 1c show typical EBSD observations of the coarse-grained and fine-grained samples, respectively, indicating their significantly different grain sizes and variation in preferred crystalline orientation.

2.2. In-situ neutron diffraction

An ENGIN-X neutron diffractometer (Rutherford Appleton Laboratory, ISIS, UK) was employed to conduct in-situ neutron diffraction measurements while coarse-grained and fine-grained samples were subjected to compression at room temperature. Fig. 2 shows a schematic diagram of the experimental setup; details of the techniques used can be found elsewhere [23]. The sample to be analysed was mounted horizontally on a stress rig (INSTRON, 100 kN) with the loading axis oriented 45° to the incident neutron beam. Two detectors (bank 1 and bank 2) were used to collect the diffraction signals at scattering angles of $2\theta = \pm 90°$, under which the diffraction vectors were parallel to and perpendicular to the loading direction of the sample, respectively. The longitudinal direction of the sample was parallel to the compression loading direction, in order to measure the longitudinal lattice strain component. The neutron scattering gauge volume was 4 × 4× 4 mm^3, which was defined by the 4 × 4 mm^2 incident slit, and the 4-mm wide receiving collimators. When the sample was compressed in a step-wise manner, the neutron data was collected at intervals of 20 min. Two different loading methods were applied during the compression experiment. First, the sample was compressed under the stress-control mode (stress holding) to a level of 350 MPa with a step of 50 MPa and a loading rate of 10 MPa/s. Then the sample was deformed under the displacement-control mode (strain holding), allowing a specific compression speed to be achieved. Both types of samples were tested using a compression rate of 0.5 mm/min during the displacement-control deformation. The diffraction spectra were analyzed using the Open Genie software package which provides *d*-spacing (*d*), peak intensity (*I*), and full width at half maximum (*FWHM*).

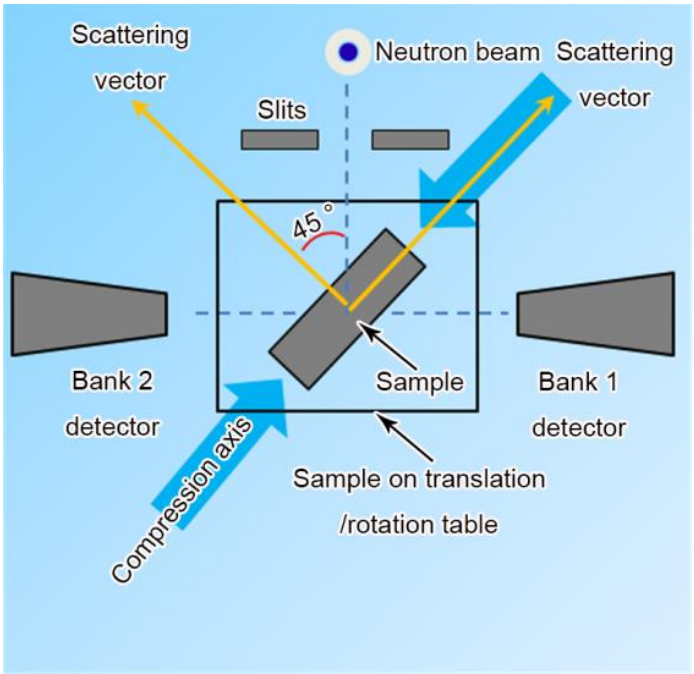

Fig.2 Schematic representation of the in-situ neutron diffraction experimental setup at ENGIN-X, ISIS, UK.

2.3. Microstructure characterisation

Bulk samples of 10 mm in height, 12 mm in length and 3 mm in width, were cut from the top and middle regions into transverse direction (TD)-longitudinal direction (LD) cross-sections before and after compression in both coarse-grained and fine-grained samples. A bulk sample schematic of the Inconel 625 alloy is shown in Figs. 3a and b. The samples for EBSD analysis were first prepared through a standard procedure of metallographic grinding and polishing to obtain a mirror finished surface. Samples were then electron-polished in a solution of 80% methanol and 20% H_2SO_4 at 20 V for 30 s at room temperature. EBSD measurements were made using a fully automated EBSD system attached to a Quanta 450 field-emission gun scanning electron microscope (FEG-SEM). The EBSD facility was equipped with a Nordlys EBSD detector to collect backscattered electron signal. EBSD scanning was performed on the top region over an area covering 1000 μm × 2000 μm, and on the middle region, over an area covering 1000 μm × 1000 μm. A step size of 2 μm was employed for samples in the as-received condition. The acquired EBSD data were exported to Channel 5 software for post-processing analysis. Orientation imaging microscopy (OIM) images and the misorientation angle of grains and sub-grains were then calculated from the EBSD results. The density of geometrically necessary dislocations (GND) and the strain localisation in this study were analszed using the Kernel average misorientation (KAM) [24-25].

TEM studied were conducted on the top region of samples using an FEI Talors F200 TEM operated at 200 kV to examine the sub-structure of samples after in-situ neutron diffraction experiments. TEM samples were cut from the top region of the deformed samples and then carefully ground to a thickness of 50 μm, followed by ion thinning using a Gatan 695 precision ion polishing system.

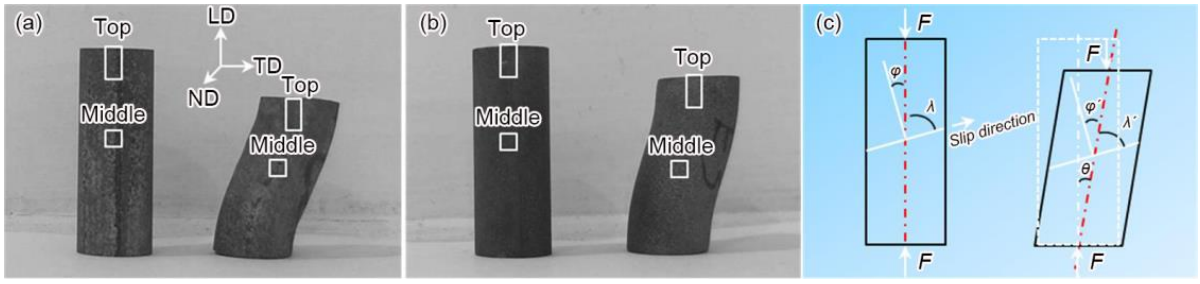

Fig.3 Inconel 625 alloy shape before and after compression for a (a) coarse-grained and (b) fine-grained sample; (c) rotation of the crystal in crystal compression (*F*—applied force; ϕ, ϕ'—angle between normal line of slip plane and central axis of applied force *F*; λ, λ'—angle between slip direction and applied force *F*; θ—rotation angle of central axis of applied force *F*.). (LD—longitudinal direction; the two directions perpendicular to the LD are indicated as normal direction (ND) and transverse direction (TD))

3. Results

3.1. Macro stress and strain curves

Fig. 4 shows the macro stress-strain curves and the work-hardening rate curves obtained during the compression deformation tests. In Fig. 4a, a typical strain relaxation phenomenon was observed in both the coarse-grained and fine-grained samples before the applied stress reached 350 MPa, which was attributed to the stress-control mode (stress holding) during in-situ neutron

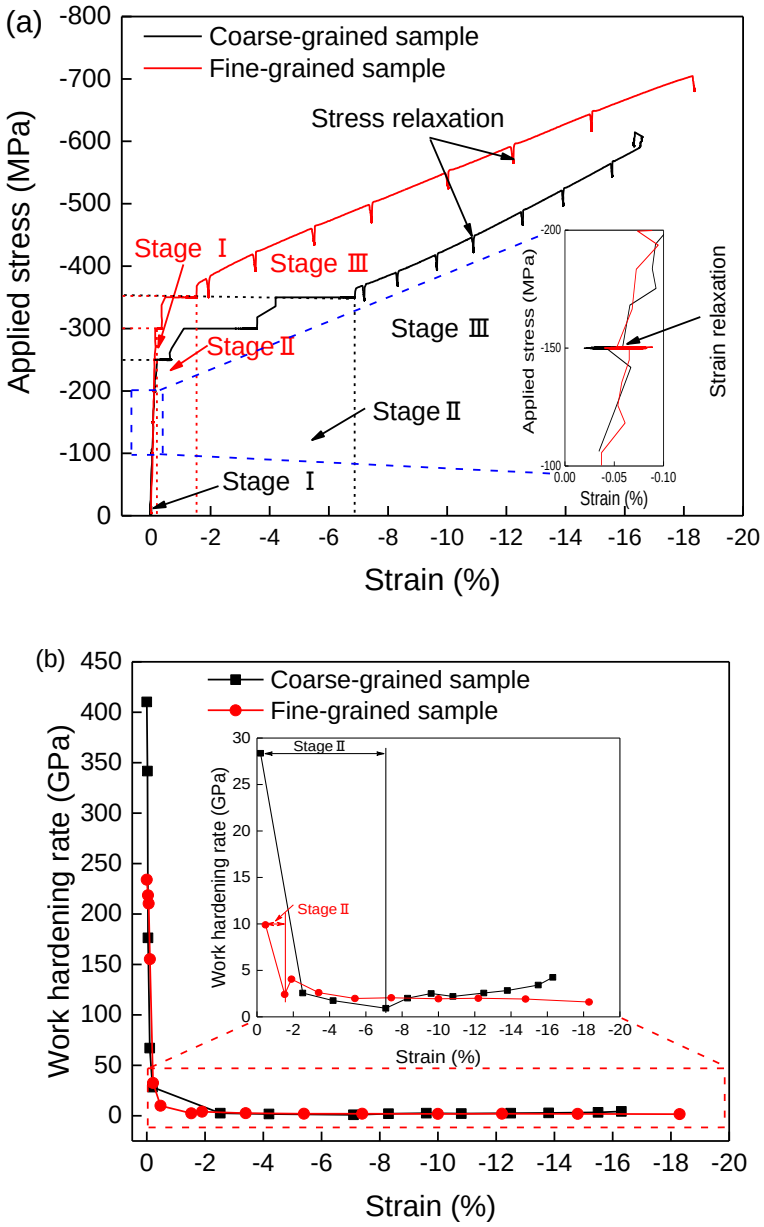

Fig.4 (a) Macro stress-strain curves of coarse-grained and fine-grained samples during compression at room temperature and (b) the work-hardening rate curve.

diffraction measurement period. A typical stress relaxation phenomenon was observed in both samples after applied stress was higher than 350 MPa, which was attributed to displacement-control mode (strain holding) during the in-situ neutron diffraction measurement period. It is a typical strain and stress relaxation phenomenon that can also be found in Mg alloy during in-situ neutron diffraction measurement [26]. Meanwhile, the compression deformation of the coarse-grained and fine-grained samples can be divided into three stages: (1) the elastic deformation region (stage I, $\sigma_c \leq 250$ MPa, $\sigma_f \leq 300$ MPa, here, 'c' denotes coarse-grained and 'f' denotes fine-grained); (2) the elasto-plastic transition region (stage II, 250 MPa $< \sigma_c \leq 350$ MPa, 300 MPa $< \sigma_f \leq 350$ MPa); and (3) the plastic deformation region (stage III, $\sigma_c > 350$ MPa, $\sigma_f > 350$ MPa). At stage I, the strain response was linear to the applied stress and the transition from stage I to stage II indicates the yielding strength of the tested samples. The fine-grained sample shows a yield strength of 300 MPa, higher than the coarse-grained sample by 50 MPa. The increased yield strength can be explained from the Hall-Petch relation: the yield strength of a polycrystalline materials increases with decreasing grain size [27]. In other words, the grain refinement resulted

in increased resistance of the grain boundaries to dislocation motion prior to the occurrence of plastic deformation. At stage II, the coarse-grained sample exhibited a broader elasto-plastic transition region than the fine-grained sample, indicating that the fine-grained sample experienced more work-hardening during contraction and thus achieved a smaller amount of contraction compared to the coarse-grained sample (Inset in Fig. 4b). At stage III, the strain response to the applied stress became linear again. Meanwhile, both samples showed similar work-hardening trends (Fig. 4b), but the coarse-grained sample shows slightly higher work hardening rate at higher strains. In brief, the compression tests revealed that, the grain refinement not only made the deformation more homogeneous (narrow elasto-plastic transition region) but also enhanced the yield strength of the Inconel 625 alloy.

After the compressive deformation experiment, both samples presented S-shape deformation (Fig. 3). This phenomenon is believed to be related to grain rotation and free deformation during compression [27]. More details discussing the grain rotation are included in the results from neutron diffraction and EBSD analyses.

3.2 Neutron diffraction analysis

3.2.1. Evolution of diffraction peak position

Fig. 5 shows neutron diffraction patterns of the coarse-grained and fine-grained samples at various stress/strain levels. For the coarse-grained sample, the (200) peak is not initially visible which is related to initial orientation of the different grains, until the strain reached -10.8 % (Fig. 5a). Then, the {200} peak became increasingly strong with increasing strain. Meanwhile, Fig. 5a also indicates the variation of other diffraction peaks, such as the decreasing intensity of the {111} and {220} peaks and increasing intensity of the {311} peak with increasing strain. Fig. 5b highlights the variation observed for the {111} peak. These diffraction peak variations were attributed to continuous changes of the number of grains, which favoured the generation of a diffracted neutron beam with respect to the direction of the incident neutron beam. In other words, the changing diffraction patterns suggest compression induced grain rotation of the polycrystalline sample.

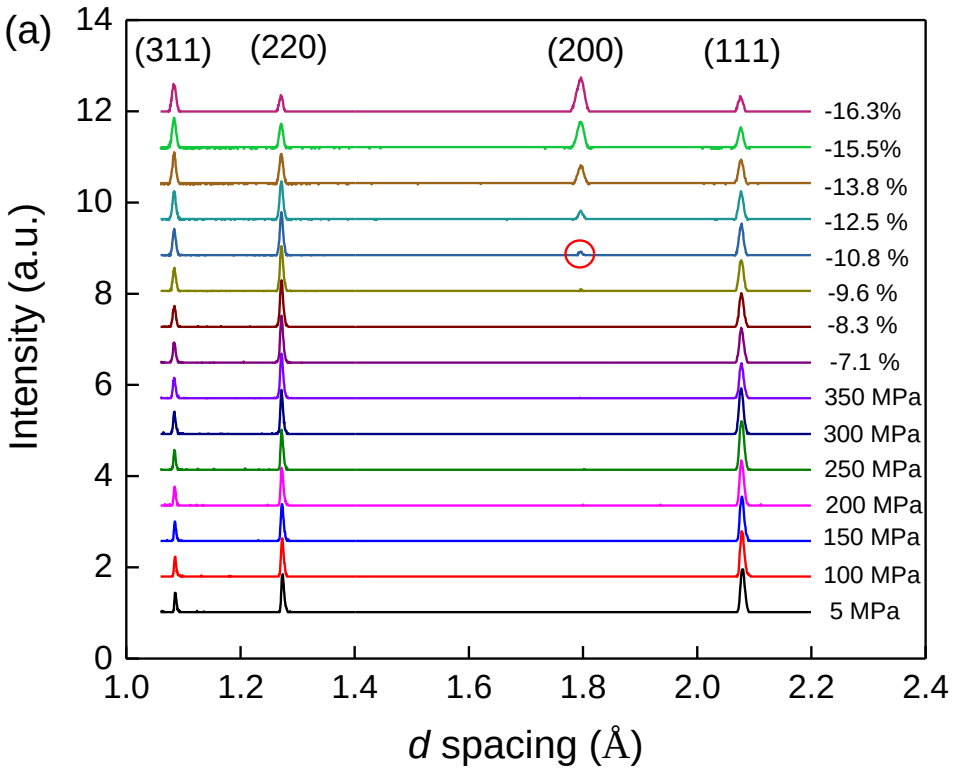

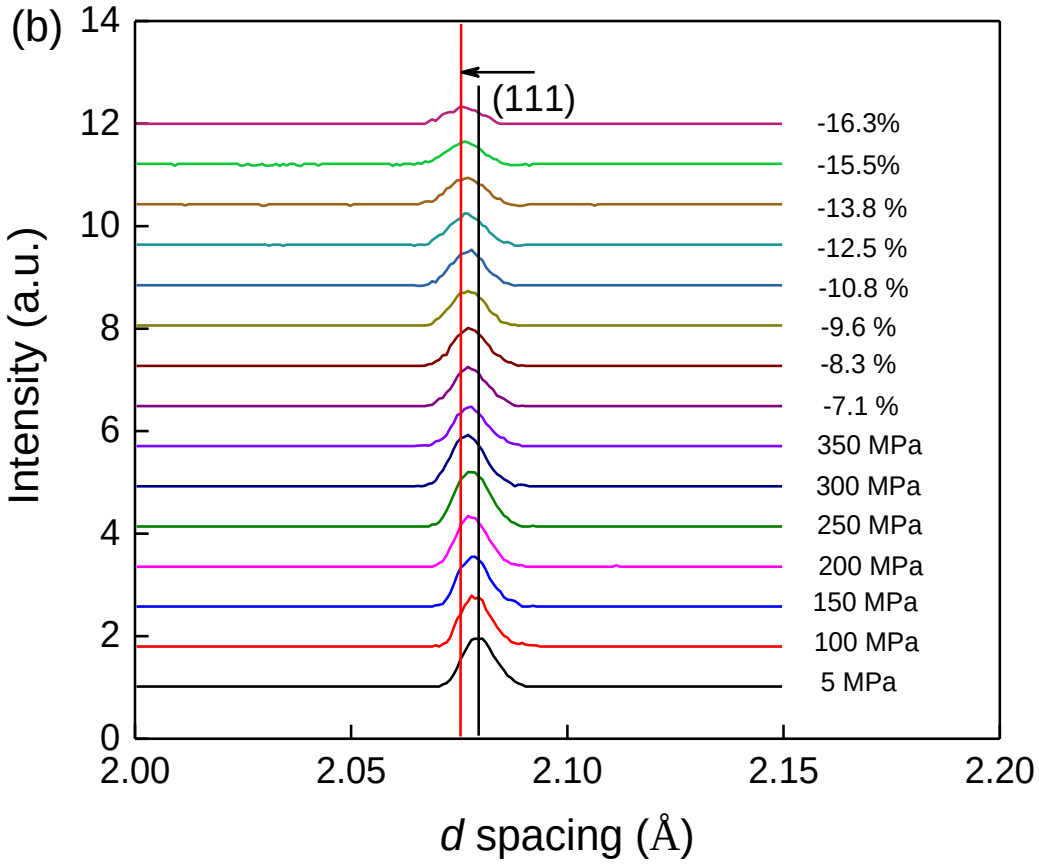
(b)
(111)
-16.3%
-15.5%
-13.8 %
-12.5 %
-10.8 %
-9.6 %
-8.3 %
-7.1 %
350 MPa
300 MPa
250 MPa
200 MPa
150 MPa
100 MPa
5 MPa
Intensity (a.u.)
d spacing (Å)

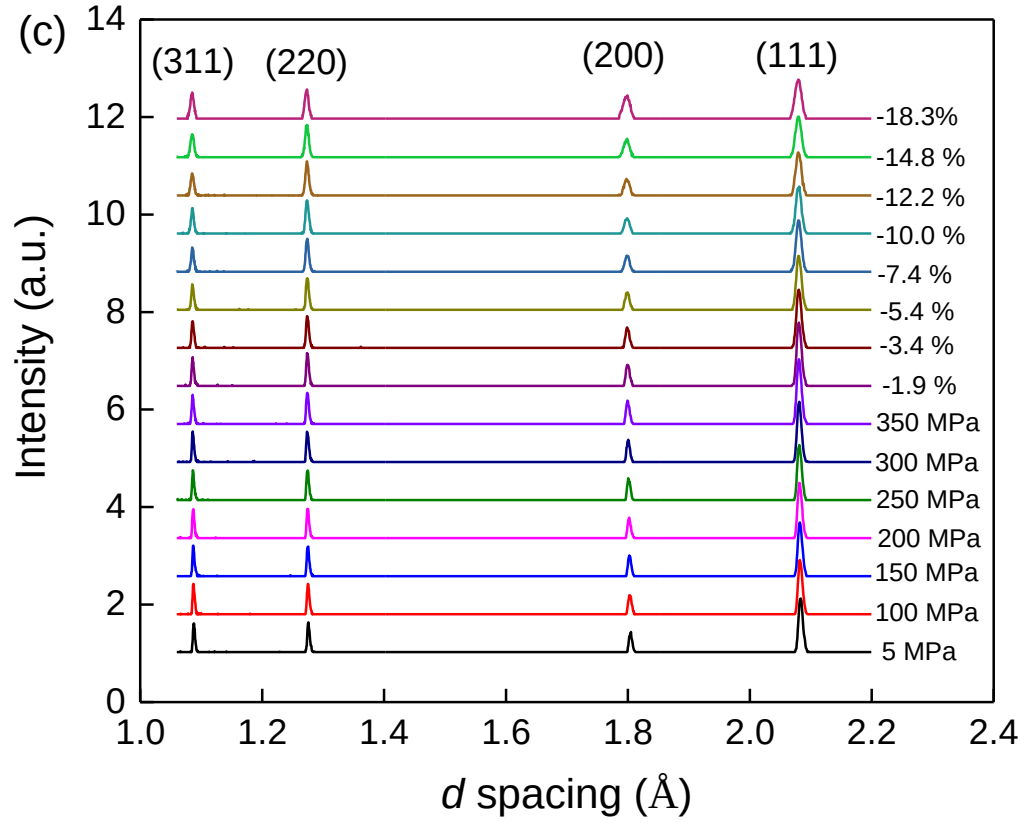
(c)
(311)
(220)
(200)
(111)
-18.3%
-14.8 %
-12.2 %
-10.0 %
-7.4 %
-5.4 %
-3.4 %
-1.9 %
350 MPa
300 MPa
250 MPa
200 MPa
150 MPa
100 MPa
5 MPa
Intensity (a.u.)
d spacing (Å)

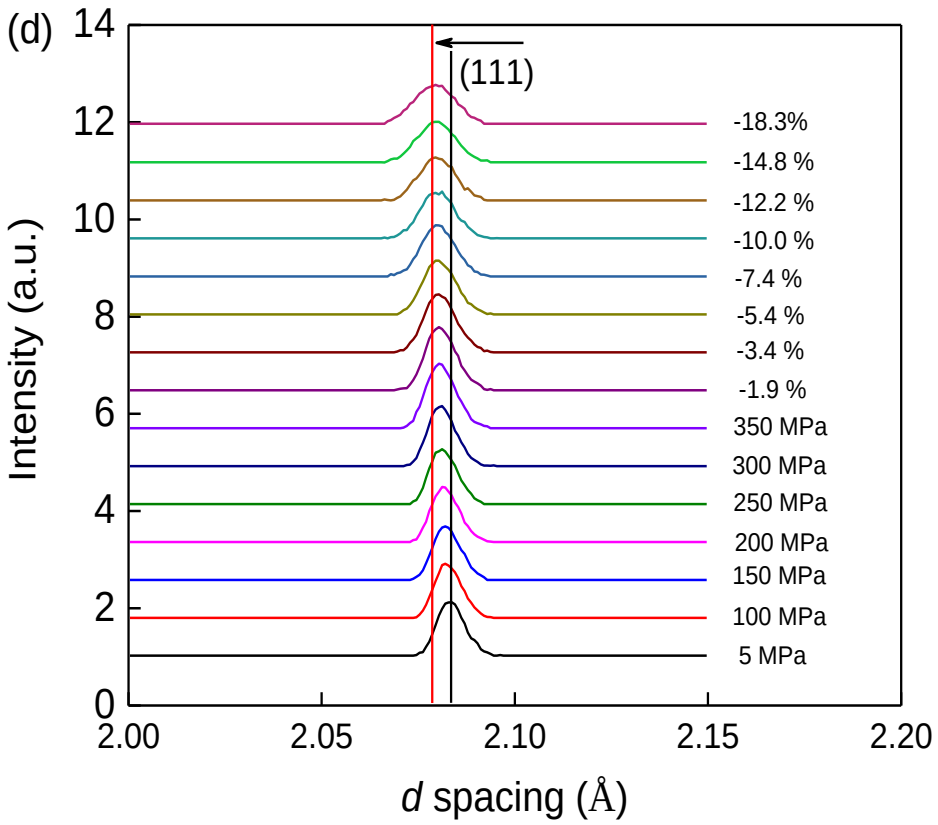

Fig.5 Diffraction pattern evolution of (a) coarse-grained and (c) fine-grained samples during compression at room temperature: (b) and (d) are enlarged images of the corresponding (111) peak in Fig. 5(a) and (c), respectively.

Similar variations of diffraction peaks were also observed in the fine-grained sample, as shown in Fig. 5c. Moreover, the diffraction patterns of the fine-grained sample differ from those of the coarse-grained sample; the former showed all four diffraction peaks during the entire compression period, including (111), (200), (220), and (311) peaks. This diffraction behaviour can be attributed to the increased number of grains in the fine-grained sample as compared to the coarse-grained sample.

In addition, the diffraction analyses also revealed marginal shifting of the diffraction peaks with increasing compression strain. The diffraction peak positions of the coarse-grained and fine-grained samples shifted to lower *d*-spacing with strain or stress increases (Figs.5b and d). The lattice parameters of both samples held at 5 MPa were obtained via whole pattern fitting using Pawley refinement. The results are listed in Table 2, indicating that grain refinement slightly increased the lattice parameter.

Table 2 Lattice parameter (α_0) and diffraction elastic moduli (E_{hkl}) of coarse-grained and fine-grained samples.

Inconel 625 alloy	α_0 (nm)	E_{111} (GPa)	E_{220} (GPa)	E_{311} (GPa)	E_{200} (GPa)
Coarse-grained	0.3603	252.4 ± 6.7	219.3 ± 10.8	167.7 ± 13.7	-
Fine-grained	0.3626	261.2 ± 7.2	242.1 ± 6.2	199.5 ± 4.2	145.2 ± 7.2

3.2.2. The evolution of lattice strain

Lattice strains of the individual (*hkl*) orientations were calculated from their corresponding *d*-spacings according to Equation [29]:

$$\varepsilon_{hkl} = \frac{d_{hkl} - d^0_{hkl}}{d^0_{hkl}} \quad (1)$$

where ε_{hkl} and d_{hkl} are the lattice strain and lattice spacing of the {*hkl*} plane, respectively. d^0_{hkl} is the stress-free lattice spacing, which was taken from the measurement point at 5 MPa at room temperature. The *hkl*-specific lattice strains of the coarse-grained and fine-grained samples were calculated based on Eq. (1). Fig.6 shows the lattice strain evolutions as a function of the applied strain for coarse-grained and the fine-grained samples. It is clearly seen that the lattice strains in the fine-grained sample were higher than those in the coarse-grained sample. This indicates higher strength of the fine-grained sample. In Fig.6a, the (111) grains of the coarse-grained sample exhibit the lowest lattice strain at yielding point, followed by (220), and then (311). However, the (111) grains of the fine-grained sample exhibit the lowest lattice strain at yielding point, followed by (220), (311), and then (200), as shown in Fig.6b. It is indicated that the (111) grains yield first in the both samples during plastic deformation. At stage II and III, the lattice strains of the fine-grained sample increased continuously (Fig.6b). However, in the coarse-grained sample the (220) and (311) lattice strains increased continuously at stage II and III, while the (111) lattice strain increased first and then decreased at stage II, and increased continuously at stage III (Fig.6a). This reveals an anisotropic microscopic elastic and plastic deformation behaviour.

From Fig. 6, it can be also seen that the stress redistribution is different between the coarse-grained and fine-grained alloys. For the fine-grained sample, the (220) and (111) lattice strains seem to be close to each other in the initial deformation period and the (220) and (111) lattice strains gradually separate from each other with increasing strain. However, for the coarse-grained sample, the (220) and (111) lattice strains separate from each other in the deformation period. Meanwhile, the (220) and (311) lattice strains in both samples showed similar trends with increasing strain, but the coarse-grained sample shows very close with each other at higher strains. The above results indicate that the stress redistribution of the (111) and (220) grains in the coarse-grained sample occurs immediately upon yielding, while the stress redistribution of the

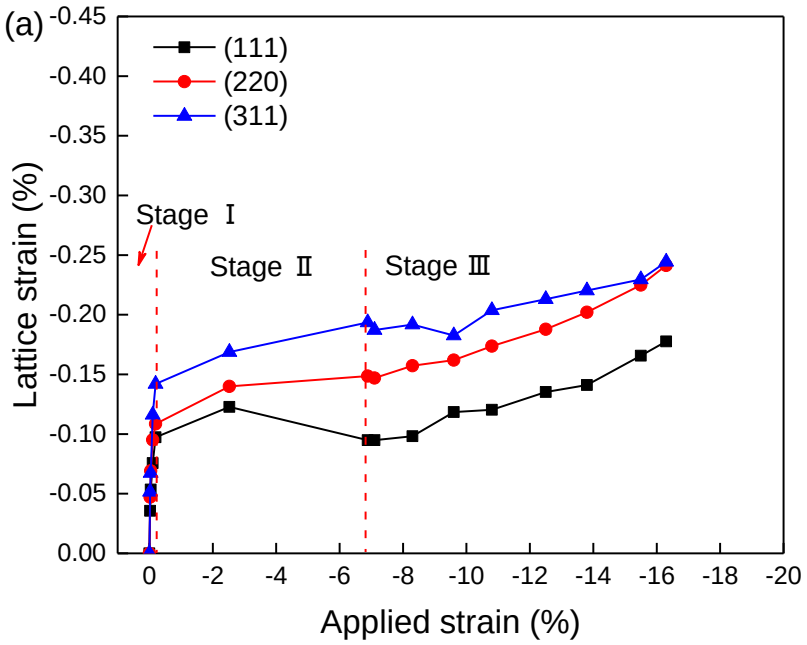

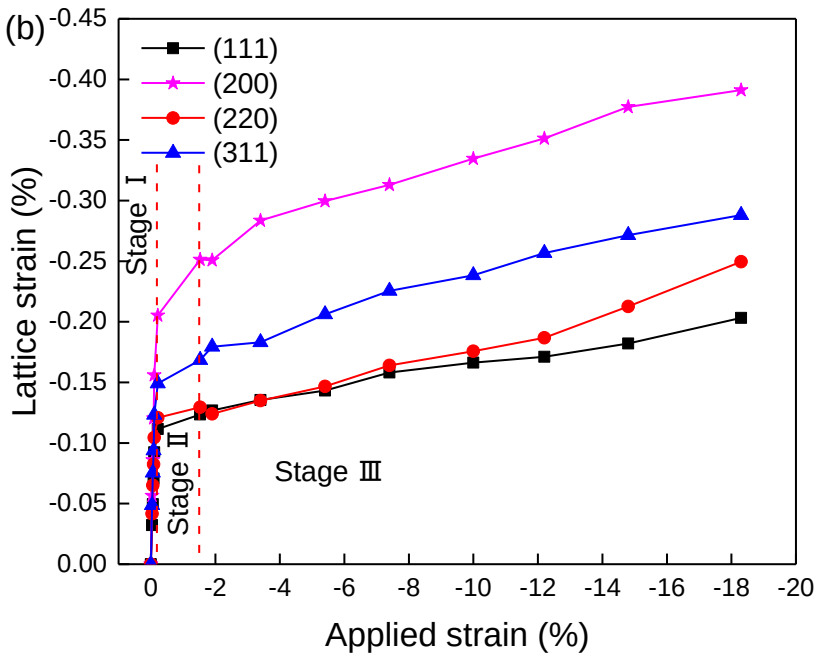

Fig.6 The evolution of lattice strains as a function of applied strain for (a) coarse-grained and (b) fine-grained samples during compression at room temperature.

(111) and (220) grains in the fine-grained sample occurs at higher strains or stresses. In other words, the coarse-grained sample shows significant stress redistribution during plastic deformation, while the fine-grained sample is no significant stress redistribution during plastic deformation. It is closely related to different orientations of the grains [30]. It is because that the finer grains are, the greater the number grains are, in the same volume of sample. The more grains with more favorable orientation during plastic deformation, thereby the better co-deformation between grains occurs. The internal stress is evenly distributed, leading to the no significant stress redistribution. Coarse grains are on the contrary.

According to Holden et al.[31], the intergranular strains were obtained by subtracting the initial elastic part from the lattice strain from the measured lattice strain. The *hkl*-specific intergranular strains of the coarse-grained and fine-grained samples were calculated based on the *hkl*-specific lattice strain data from Fig.6. Fig.7 shows the intergranular strain evolutions as a function of the applied strain for coarse-grained and the fine-grained samples. The changes in *hkl*-specific intergranular strain provide an anisotropic plasticity during the plastic deformation. The changes in intergranular strain provide develop of plastically and elastically anisotropic of material during the deformation, a material which is plastically and elastically isotropic would exhibit zero intergranular strain for all stress values [30,31]. It is noted that the intergranular strains exhibit a compressive deviation in the both samples, except for the (111) grains showing a tensile deviation in the coarse-grained sample.

Fig.8a and Fig.8b show the lattice strain evolutions as a function of the applied stress for the coarse-grained and the fine-grained samples. In stage Ⅰ, all the lattice strains respond linearly to the applied stress. The slopes provide the diffraction elastic moduli, E_{hkl}, of each (*hkl*) grain orientation, as shown in Fig.8c and Fig.8d. The determined E_{hkl} values are listed in Table 2. The (200) grains exhibit the smallest modulus, followed by (311), (220), and then (111), which is consistent with the Inconel 625 alloy elastic anisotropy reported by Wang et al. [32]. In stage Ⅱ, the lattice strain of the (111) grains in the coarse-grained sample becomes nonlinear to the

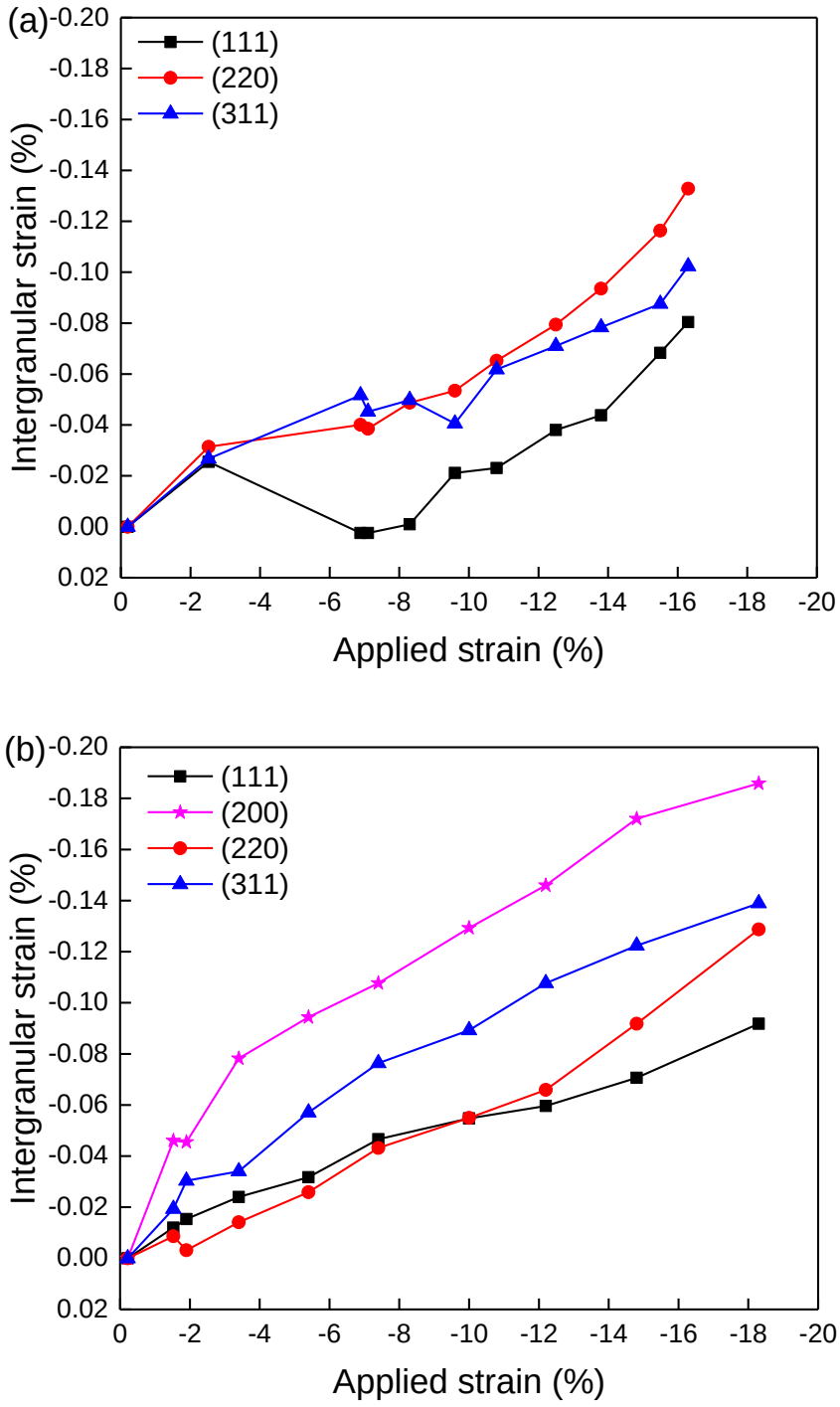

Fig.7 The evolution of intergranular strains as a function of applied strain for (a) the coarse-grained and (b) the fine-grained samples during compression at room temperature.

applied stress, which refers to the elasto-plastic transition as shown in Fig.4a. This is because the load is redistributed plastically from “softer” grain families (e.g., (111)) to “harder” grain families (e.g., (200)) [33]. In stage III, the lattice strains respond linearly to the applied stress again, except for the (311) grains in the coarse-grained sample. It has been reported that the lattice strain increases linearly again with gradients by combination of elastic and plastic anisotropy when all grains deform plastically [34]. Overall, the observed linear stress-strain relationships suggest that all the grains of the fine-grained sample are plastically deformed. The grain refinement has improved the inter-grain deformation compatibility and the deformation homogeneity.

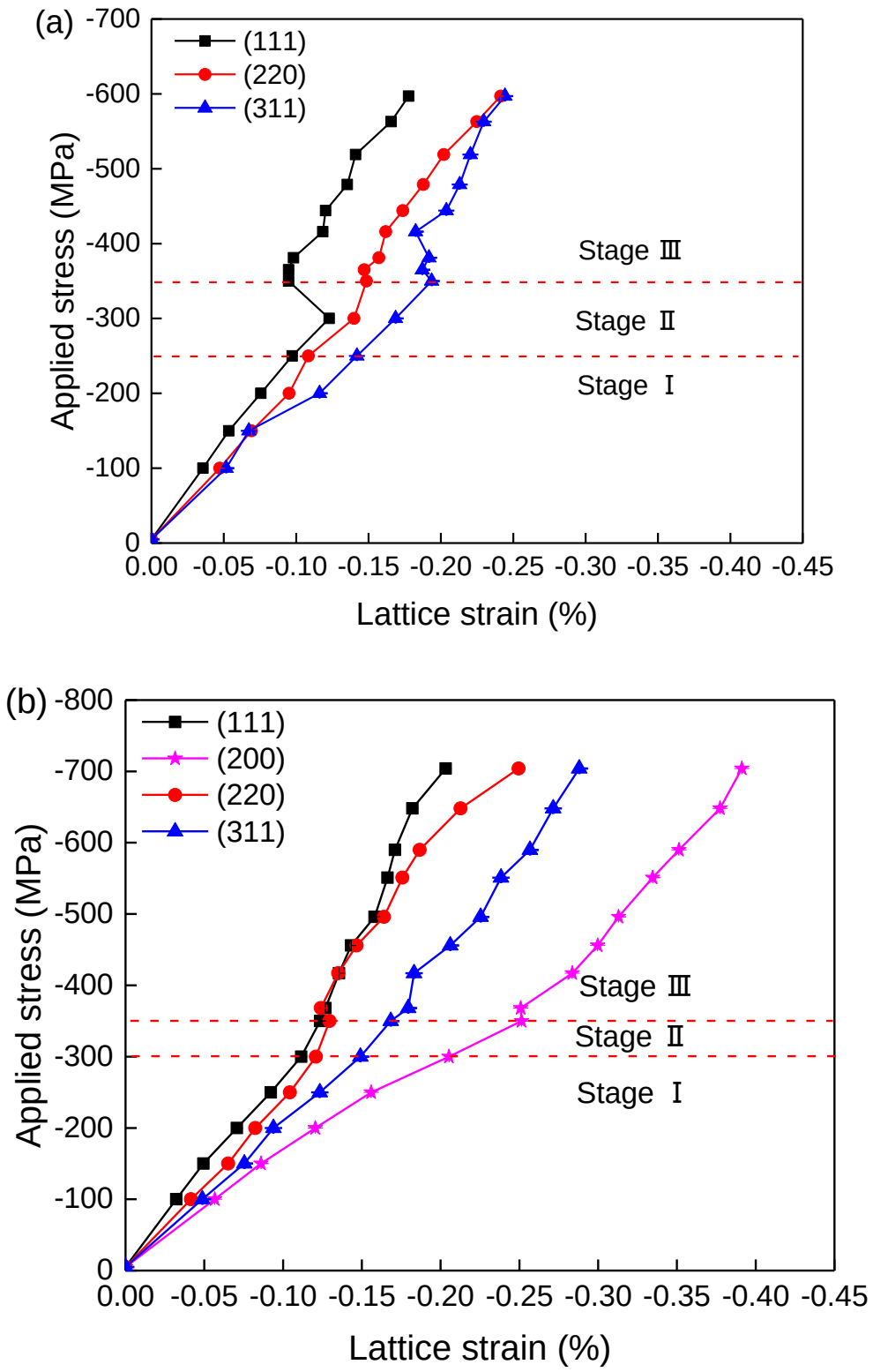

Fig.8 The evolution of lattice strains as a function of applied stress for (a) the coarse-grained and (b) the fine-grained samples during compression at room temperature: (c) and (d) are enlarged images corresponding to the evolution of lattice strain at elastic deformation in Fig. 8(a) and (b), respectively.

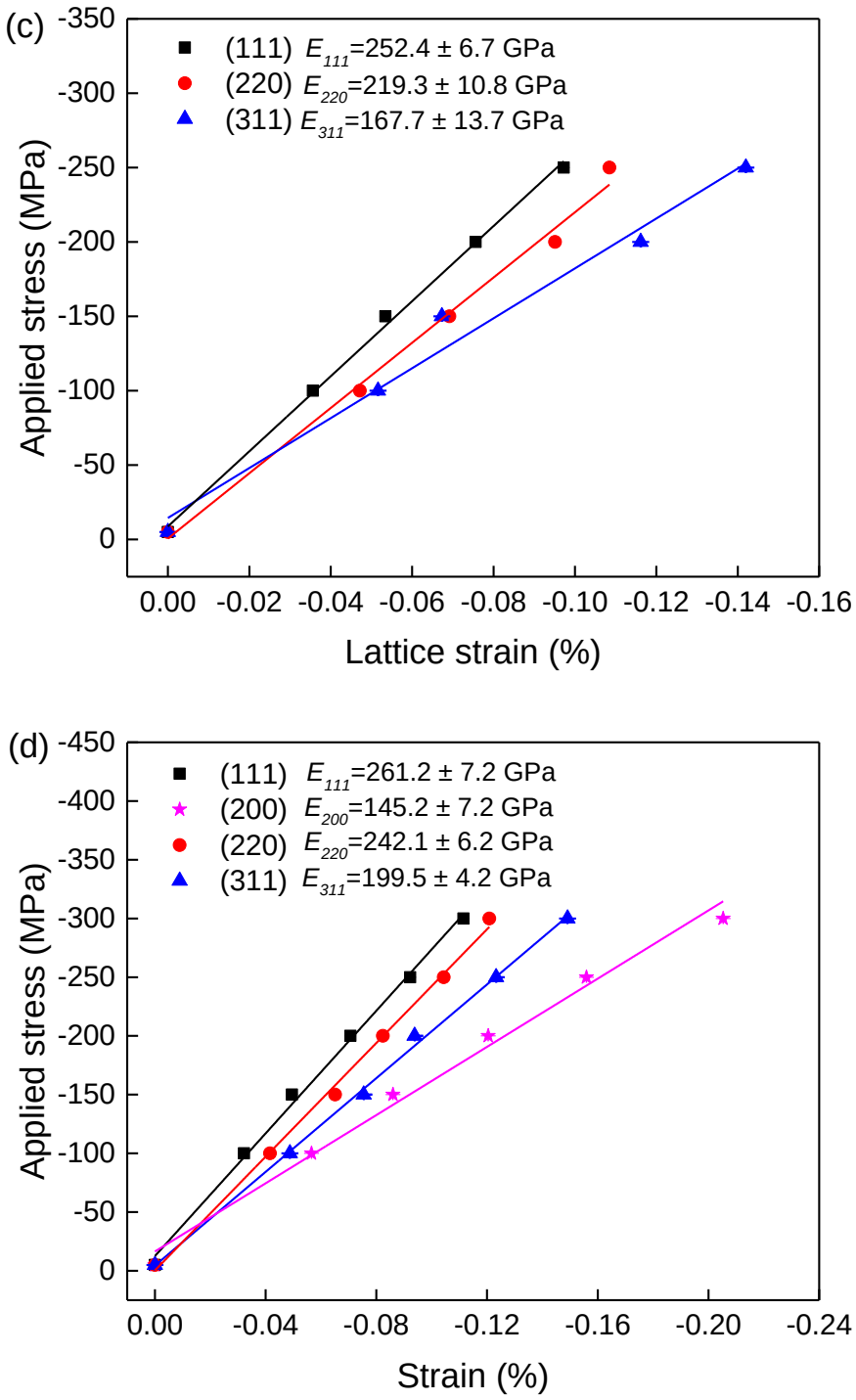

Fig.8 The evolution of lattice strains as a function of applied stress for (a) the coarse-grained and (b) the fine-grained samples during compression at room temperature: (c) and (d) are enlarged images corresponding to the evolution of lattice strain at elastic deformation in Fig. 8(a) and (b), respectively.

3.2.3. The evolution of peak intensity

Fig.9 shows the evolution of normalized integrated intensity (I/I_0) as a function of the applied stress for the coarse-grained and the fine-grained samples. The changes in integrated intensity of peaks provide qualitative insights into grain reorientation during the plastic deformation [35]. It is noted that the peak intensity remains almost constant before yielding (stage I), while the peak intensity significantly changes above yielding (stage II and III). In Fig.9a, the (311) peak shows increasing intensity by a factor of approximately 1.5, whereas the (111) peak shows decreasing

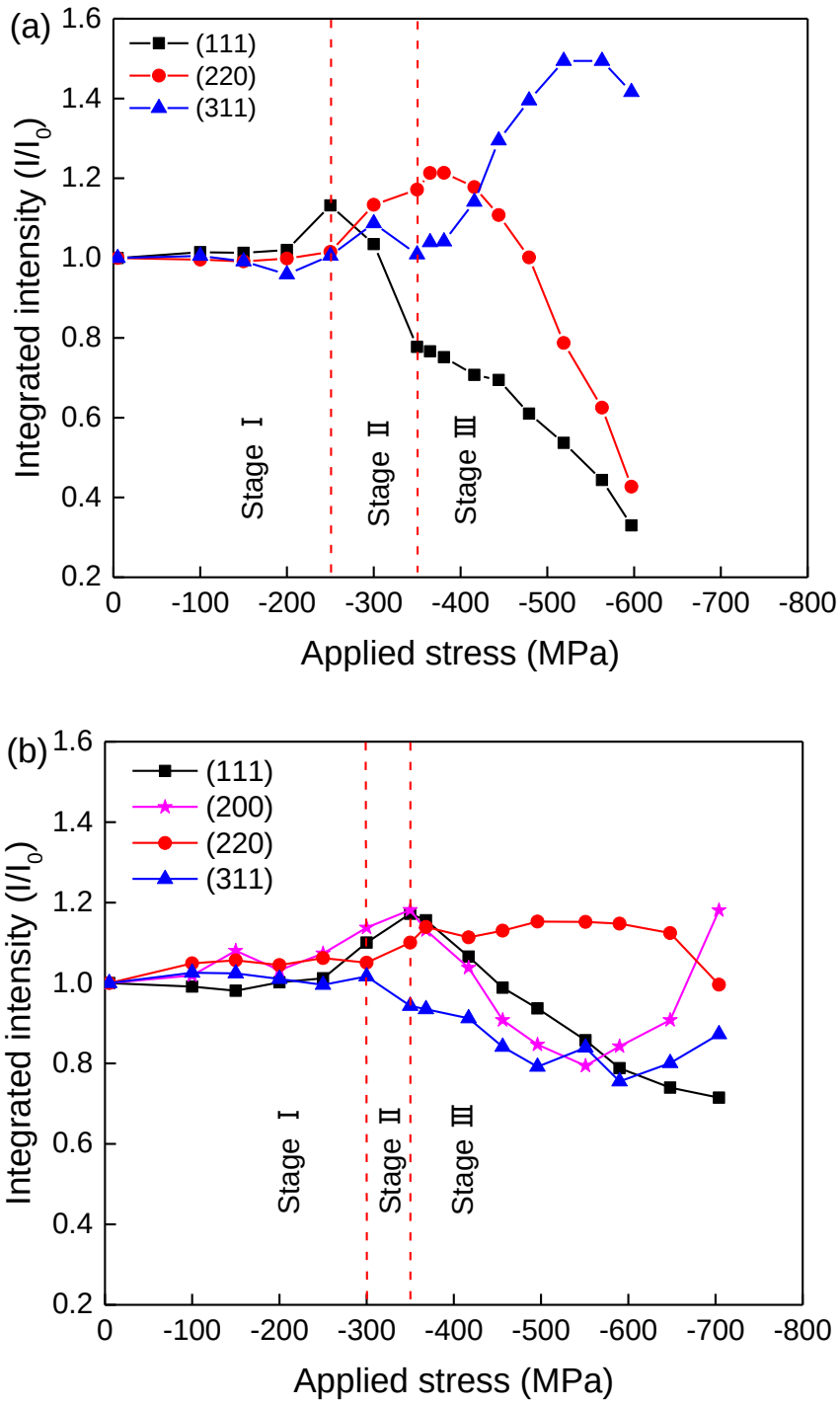

Fig.9 The evolution of normalized integrated intensities as a function of applied stress for (a) the coarse-grained and (b) the fine-grained samples during compression at room temperature.

intensity by approximately 0.3. In addition, the (220) peak shows increasing intensity first by approximately 1.2, and then decreasing intensities by approximately 0.4. These variations imply that the (311)-oriented grains gradual reorientation and a lot of the (111)-oriented grains rotate, while the (220)-oriented grains reorientation first and the then rotate during the plastic deformation of the coarse-grained sample. In Fig.9b, the (220) peak intensity remains almost constant while the (111) and (311) peaks decrease by a factor of 0.7. The (200) peak intensity first decreases by a factor of 0.8 and then increases by 1.2. These variations suggest that, some of the (111)- and (311)-oriented grains rotate away from the loading direction during plastic deformation of the fine-grained sample. Nevertheless, the scale of overall intensity changes of the fine-grained

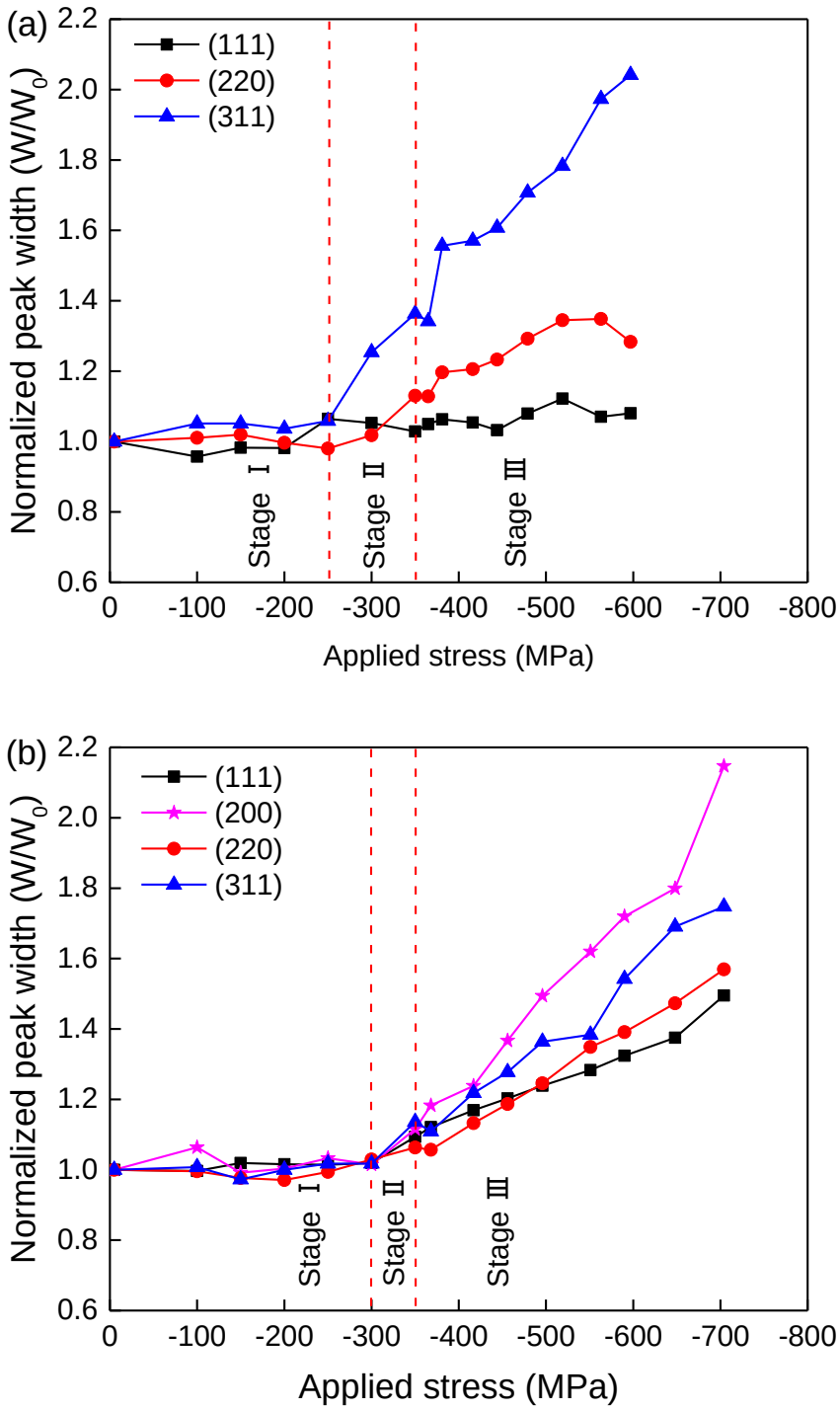

Fig.10 The evolution of normalized peak widths as a function of applied stress for (a) coarse-grained and (b) fine-grained samples during compression at room temperature.

sample is lower than that of the coarse-grained sample. This indicated that the grains of the coarse-grained sample have stronger texture and large grain rotation compared to the fine-grained sample during compression deformation.

3.2.4. The evolution of peak broadening

Fig.10 shows the evolution of the normalized peak width (W/W_0) of different (*hkl*) planes as a function of the applied stress for coarse-grained and fine-grained samples. It is noted that the peak widths remain almost constant before yielding (stage Ⅰ), while the peak widths change significantly above yielding (stage Ⅱ and Ⅲ). In Fig.10a, the width of the (311) grain family rises

by a factor of 2.1 and the (220) grain family increases by a factor of 1.3 while the (111) grain family slightly increases. In Fig.10b, the widths of the (200) and (311) diffraction peaks increase significantly by a factor of 2.1 and 1.7, respectively, whereas the widths of the (111) and (220) diffraction peaks both increase by a factor of 1.5. The pronounced peak broadening indicates strain-induced heterogeneous substructures (such as dislocations, stacking faults, and twinning) during plastic deformation of polycrystalline alloys [36-39]. This indicates that deformation in the fine-grained sample is distributed homogeneously, regardless of different grain orientations. On the other hand, deformation of the coarse-grained sample takes place preferentially in some grains, leading to more pronounced broadening of the relevant diffraction peak, i.e., the (311) diffraction.

In order to further unveil the influence of grain size on the deformation mechanism of the Inconel 625 alloy, an analysis of the neutron diffraction peak width for coarse-grained and fine-grained samples. Following the Wilkens's theory [40-42], the integral breadth of neutron diffraction peak, β_{int}, and the elastic anisotropy factor, $\Gamma_{hkl}=\frac{h^2k^2+k^2l^2+l^2h^2}{h^2+k^2+l^2}$, can be described as:

$$\beta_{\text{int}}^2=\frac{C_0}{F_i\times e^{4\pi}}(1-q\Gamma_{hkl}) \quad (2)$$

where the values of C_0 and q depend on the dislocation type, F_i is an integral factor over the Wilkens's profile which accounts for the outer cut-off radius of the dislocation strain field. Using ANIZC, we found C_0 and q to be 0.2696 and 1.4642 for the {111}<110> edge dislocations, and 0.2767 and 2.2920 for the <110> screw dislocations. Fig.11 shows the peak broadening data (β_{int}^2) as a function of the elastic anisotropy factor (Γ_{hkl}) for coarse-grained and fine-grained samples. For the coarse-grained sample, according to Fig.11a linear fit having the slope q=3.1768, which seems like a higher than the value of q for the edge and screw dislocations. It is indicated that the coarse-grained sample forms stacking faults or deformation twins during the deformation. However, for the fine-grained sample, according to Fig.11b linear fit having the slope q=1.9621,

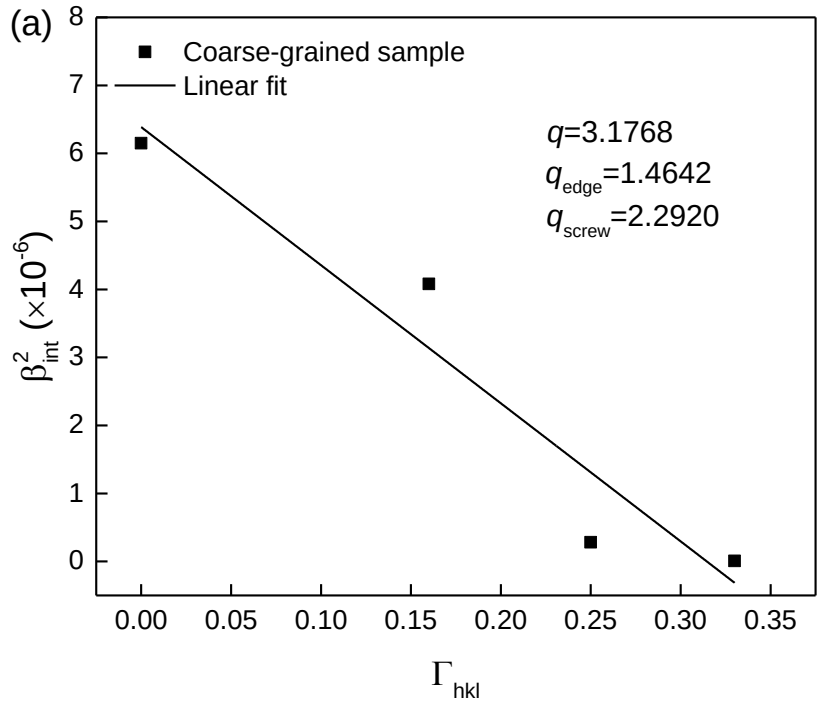

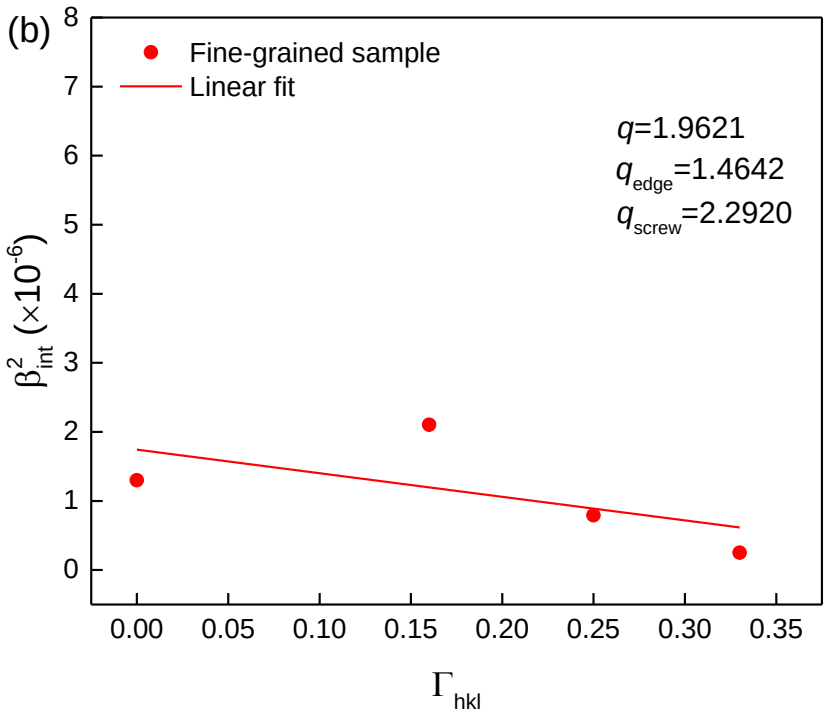

Fig.11 The peak broadening data (β_{int}^2) as a function of the elastic anisotropy factor (Γ_{hkl}) for (a) the coarse-grained and (b) the fine-grained samples during compression at room temperature.

which seems like a balancing value of *q* for the edge and screw dislocations, but close to that of the <110> screw dislocation. Thus, it is reasonable to infer that the plastic deformation of the fine-grained sample was most likely resulted from the operation of mixed of edge and screw dislocations. However, the plastic deformation of the coarse-grained sample may also form stacking faults or deformation twins, beside mixed dislocations.

3.2.5. Dislocation density

According to Liang et al. [43], the relationship between dislocation density (ρ) and average peak broadening ($\Delta d/d$) can be derived from the total elastic energy (U) and the elastic energy per unit length of dislocation (u):

$$\rho = \frac{U}{u} = \frac{15E}{2Gb^2(1+v)}\left(\frac{\Delta d}{d}\right) = \frac{15E}{2Gb^2(1+v)}\varepsilon^2 \quad (3)$$

where E is Young's modulus (E = 205 GPa), G is shear modulus (G = 79 GPa), v is Poisson's ration (v = 0.308), b is the Burgers vector (b = 0.253 nm), and ε is the average lattice strain. Based on Eq. (3), the dislocation densities (ρ) of the coarse-grained and the fine-grained samples were calculated and are shown in Fig. 12a as a function of applied stress. It is clearly seen that the two samples exhibit similar dislocation density in the elastic regime. However, differentiation between the two samples becomes apparent when the applied stress is higher than -300 MPa, i.e., corresponding to the yielding period (stage II) shown in Fig. 4. After that period, the fine-grained sample exhibits a large dislocation density than its counterpart after yielding. According to Taylor-model [44], the contribution of dislocation strengthening of the coarse-grained and fine-grained samples during the plastic deformation (stage II and III) were calculated and shown in Fig.12b. It is clearly seen that the relationship between $\rho^{1/2}$ and applied stress of the fine-grained sample is conforms to the Taylor relationship. While the relationship between $\rho^{1/2}$ and applied stress of the coarse-grained sample is deviates from the Taylor relationship which is related to

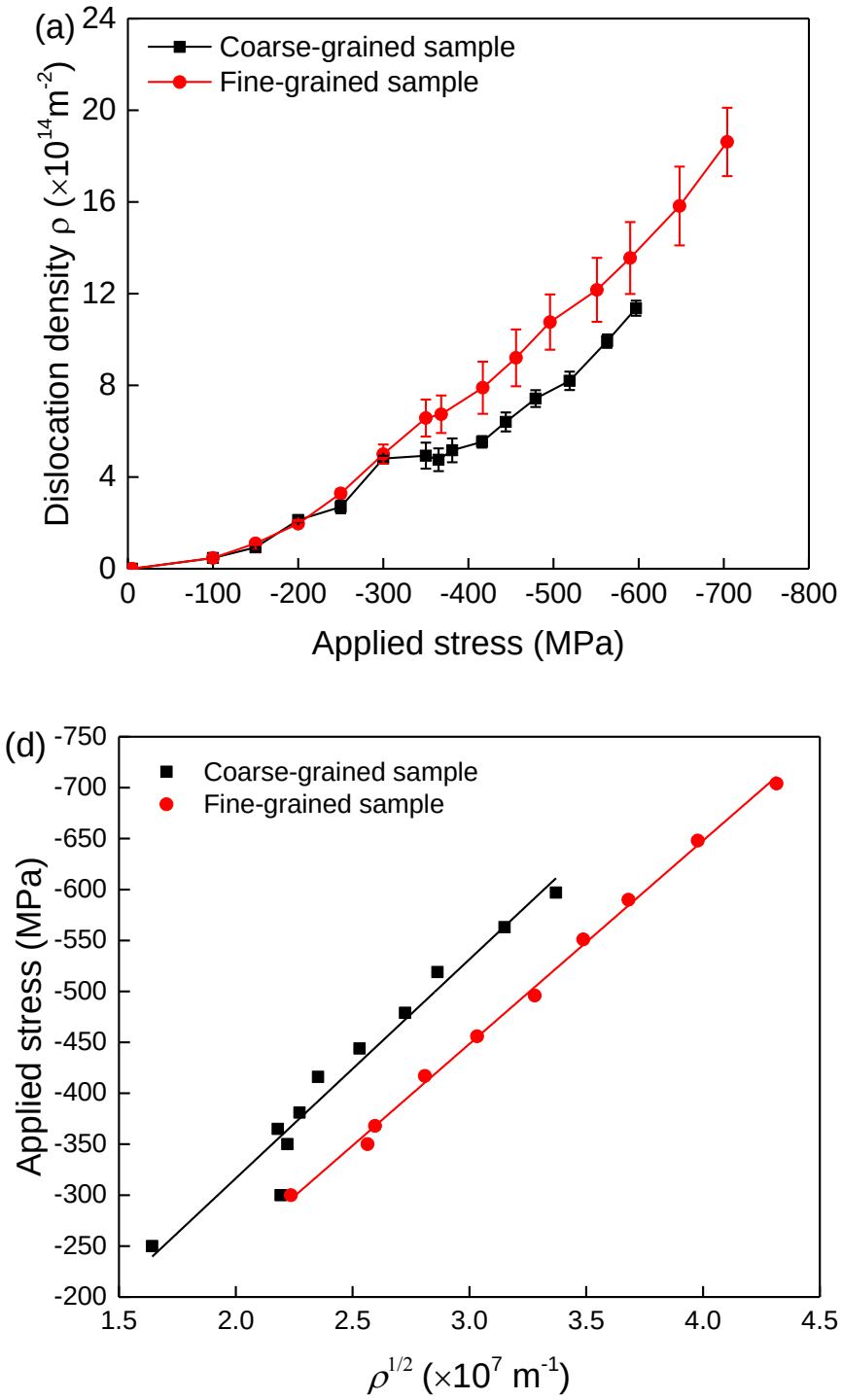

Fig.12 The evolution of dislocation density as a function of applied stress (a) and the contribution of dislocation strengthening (b) for the coarse-grained and the fine-grained samples.

the formed of stacking faults and twins during the plastic deformation. This indicates that the work hardening of the fine-grained sample is dominated by dislocation strengthening, while the work hardening of the coarse-grained sample has an additional strengthening mechanism besides dislocation strengthening, which result is consistent with inset in Fig. 4b.

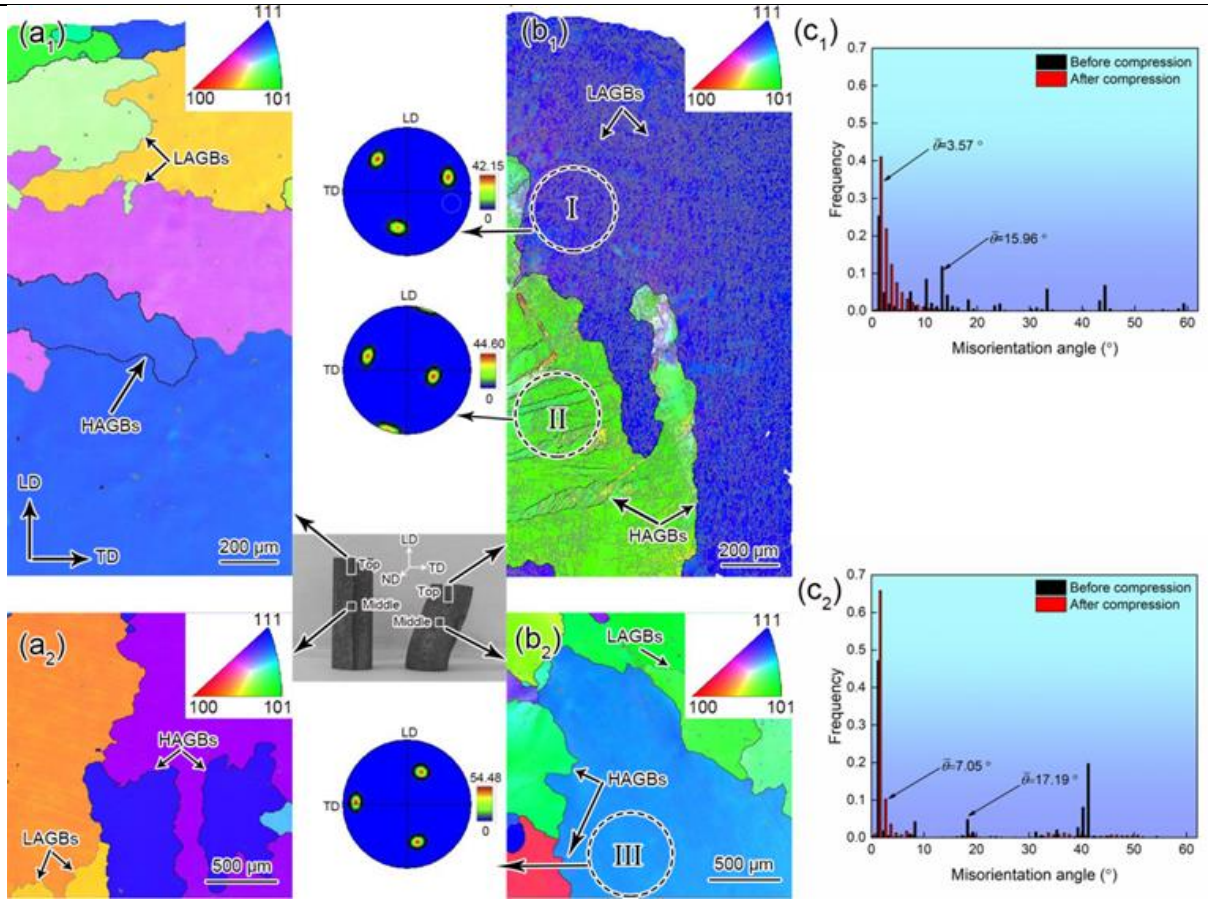

Fig.13 Microstructures of the coarse-grained sample before and after compression in the top and middle regions: (a_1) and (a_2) are IOM maps before compression; (b_1) and (b_2) are IOM maps after compression; (a_1) and (b_1) are the top region and (a_2) and (b_2) are the middle region; (c_1) is the misorientation angle distribution map before and after compression in the top region; (c_2) is the misorientation angle distribution map before and after compression in the middle region.

3.3. Deformed microstructures

3.3.1. Deformed microstructure of the coarse-grained sample

The deformed microstructures of the two samples, after the in-situ neutron experiment, were analyzed using EBSD and TEM to reveal the effect of grain size on the deformation mechanism. Fig.13 shows EBSD analyses of coarse-grained sample microstructures in both the top and middle regions, before and after the compression experiment. The gray lines in Fig. 13 indicate low-angle-grain boundaries (LAGBs, $2° < \theta \leqslant 15°$), whereas the black lines reveal high-angle-grain boundaries (HAGBs, $\theta > 15°$). Figs.13a_1 and 13a_2 show the top and middle region microstructures, respectively, of the coarse-grained sample prior to the compression experiment. Obviously, the microstructures in these two regions are similar, with large equiaxed grains and a few fine recrystallised grains. After compression, the top region shows a dense network of LAGBs, a few HAGBs, and elongated grains within the original grains, as shown in Fig. 13b_1. The elongated grains (zone II) are perpendicular to the compression axis, indicating significant rotation during compression [45]. Similar LAGBs and HAGBs are seen in the middle region, Fig.13b_2. These results are consistent with grain rotation previously analysed by in-situ neutron diffraction. In addition, it is noticed that the deformed grains in the top region exhibit a strong Brass orientation, {110}<112>, in which the maximum density of grain orientation has reached 44.80 (zone II). The deformed grains also exhibit a weak Copper orientation, {112}<111>, where the maximum density of grain orientation is 42.15 (zone I). The formation of Brass orientation is

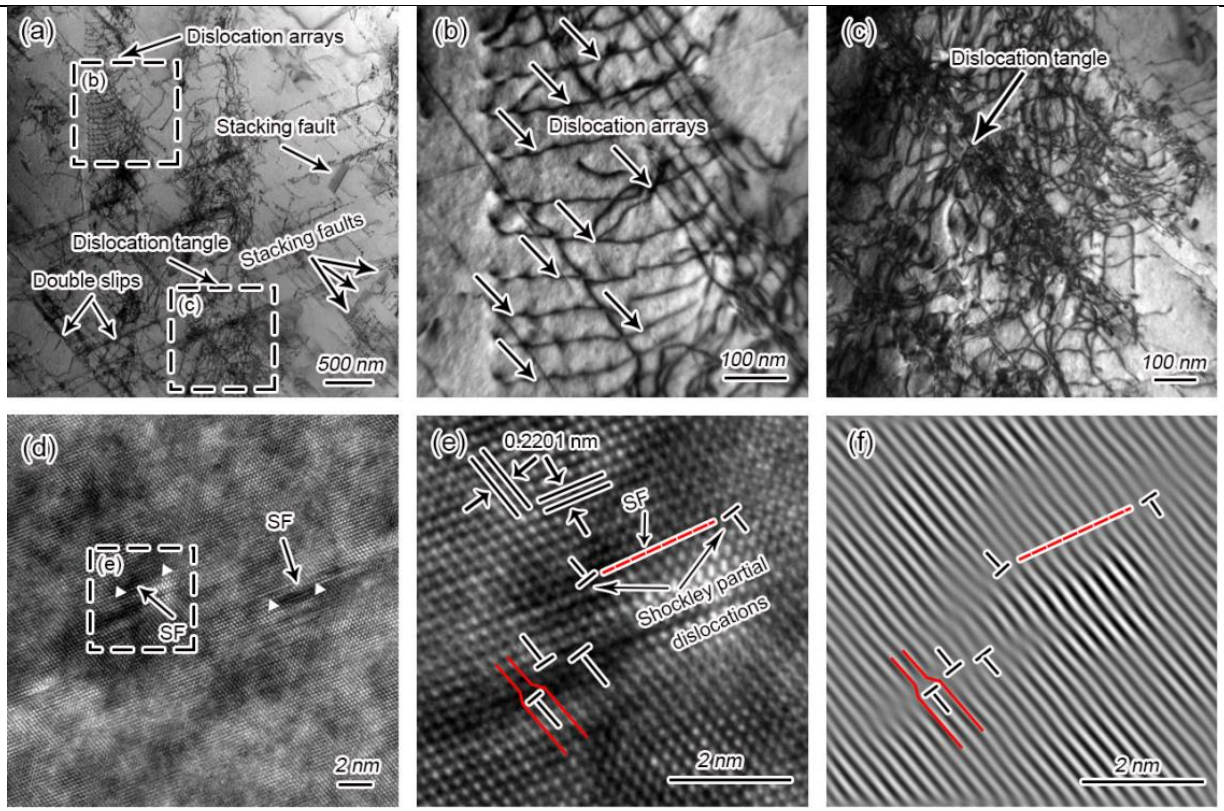

Fig.14 Typical deformed microstructure of the coarse-grained sample: (a) low magnification TEM image showing dislocations and SFs; (b-c): enlarged images showing different dislocation structures of corresponding regions in (a); (d) HRTEM micrograph showing SFs and extended dislocations; (e) enlarged HRTEM image from (d) showing individual SFs and Shockley partial dislocations; and (f) FFT image of (e), indicating the locations of SFs and Shockley partial dislocations. The SF width is approximately 1.98 nm. Edge dislocations are marked by black "T"s in (e and f).

attributed to deformation twinning, while the formation of Copper orientation is attributed to dislocation slip [46]. In contrast, the deformed grains in the middle region have a strong Rotated-Goss orientation, {110}<110>, having the maximum density of grain orientation of 58.48 (zone III). Figs. 13c_1 and 13c_2 show the misorientation angle distributions between the top and middle regions and between the non-deformed and deformed samples, respectively. These four analysed regions all exhibit a single-peak distribution profile, whereas the compressive deformation resulted in increased preference and dramatically lower misorientation angles for the coarse-grained samples. The frequency peaks correspond to GND interfaces formed by numerous dislocation tangles, which has been reported in literature [47]. During the compression process, a large number of dislocations were generated and subsequently intertwined to form dislocation tangles and GND interfaces. Thus, the HAGBs change to LAGBs in the coarse-grained sample during compression deformation.

Fig.14 shows TEM observations of the deformed microstructure of the coarse-grained sample. Fig.14a is a bright field (BF) image at a relatively low magnification, which shows the intragranular distribution of double slip lines, dislocations (mixed dislocations), and stacking faults (SFs). The results are consistent with the neutron diffraction (Fig.11a). TEM-BF observations of this sample did not indicate any twins. Meanwhile, the double slip lines cross each other to exhibit fine substructures, e.g., the highlighted areas in Figs.14b and c show the fine structures of planar dislocation arrays and compact dislocation tangles, respectively. The planar dislocation arrays and grids in Fig.14b are typical dislocation configurations that are similar to those generated in

the deformation of Inconel 600 alloy at low strains and strain rates [48]. This configuration can be attributed to the low SFE, which causes the dislocations to arrange themselves into planar arrays on their primary slip planes because of the high cross-slipping resistance of partial dislocations. Fig.12d is a high-resolution TEM (HRTEM) image showing an abundance of nano-spaced SFs, which confirms the significant role of SFs regarding deformation of the coarse-grained samples. A small area of Fig.14d, containing a stacking fault, at a higher magnification in Figs.14e and f to observe fine lattice features. Fig.12e reveals the formation of partial dislocations and SFs in the coarse-grained sample during deformation at room temperature. Fig.12f is a fast Fourier transformation (FFT) analysis of the imaged area, which clearly shows lattice distortion around the SF. Comparing the HRTEM image (Fig.12e) and the FFT image with (111) plane fringes (Fig.12f), the latter shows much more clearly the location of the SF and partial dislocations. Meanwhile, there is a SF, having a width of 1.98 nm, between two Shockley partial dislocations (Fig.12e and f). Such SFs are believed to result from the slip of Shockley partial dislocations having a Burgers vector of α/6<112> on the {111} plane [16]. In other words, the formation of SFs is related to extended dislocations, whereas an extended dislocation is known to be comprised of two partial dislocations with a SF in between. Eq. (4) expresses the conversion of a perfect dislocation to an extended dislocation [49].

$$\frac{1}{2}[1\bar{1}0] \rightarrow \frac{1}{6}[\bar{1}2\bar{1}] + \mathrm{SF} + \frac{1}{6}[\bar{2}11] \quad (4)$$

3.3.2. Deformed microstructure of the fine-grained sample

Fig.15 shows EBSD analyses of the fine-grained sample. Figs.15a_1 and a_2 show microstructures of the top and middle regions, respectively, prior to compressive deformation. The microstructures of the two regions were similar, with both consisting primarily of fine equiaxed grains regardless of the LD and TD. A few lamellar annealing twins are also visible inside some grains. The equiaxed grains were formed during static recrystallisation, i.e., the process of nucleation of low-strain grains and subsequent growth through migration of sub-grain boundaries [50]. The annealing twins were formed during grain growth by growth accidents on a migrating grain boundary [51]. After compression deformation, a large number of LAGBs within original grains in the top region were observed (Fig.15b_1). Fewer LAGBs were observed in the middle region (Fig.15b_2). Meanwhile, the fraction of twin boundaries (TBs) in the top and middle regions was reduced. Fig.15c_1 and c_2 show variation of misorientation induced by compressive deformation. For the top region of the fine-grained sample, Fig.15c_1, the misorientation angle distributions exhibit a bimodal distribution, with one peak around 1.5 ° and the other around 60 °. The misorientation angle distributions became unimodal, with a peak at approximately 1.5 °. Such variation of misorientation distributions has also been confirmed by comparative analysis of the middle region, as indicated in Fig.15c_2. Obviously, the low-angle peak corresponds to the GND interface while the peak located near 60 ° corresponds to annealing twins [52]. During the compression process, a large number of dislocations appear and intertwine to form GND interfaces, as well as a piling-up of dislocations in front of TBs [53]. Thus, the HAGBs change to LAGBs and the fraction of TBs is reduced during compression deformation.

Fig.16 shows TEM characterisation of the compression deformed fine-grained sample. In Fig.16a, slip lines and dislocations (mixed dislocations) appear in the BF image, in addition to dislocation pile-ups at the GBs. Meanwhile, the slip lines end at the GBs, which suggest the role of GBs in impeding dislocation motion. Fig.16b shows several areas of dislocation tangles and slip lines. In Fig.16c, another area shows the fine structure of planar dislocation arrays. No SFs

or deformation twins were observed during BF imaging. The above TEM observations are consistent with the neutron diffraction (Fig.11b). The results of HRTEM imaging are shown in Figs.16d ~ f. Fig.16d shows dislocations in the lattice image and the highlighted area is shown in Fig.16e at a higher magnification with a clearer lattice view. Fig.16e reveals a number of partial dislocations in the fine-grained sample. To clarify the lattice distortion around the dislocations, FFT analysis was performed in the same area and is shown in Fig.16f, revealing the location of partial dislocations. The lattice spacing on the {111} plane was measured to be 0.2548 nm, which is larger than of the coarse-grained sample (0.2201 nm). This result is consistent with that previously analyzed by neutron diffraction.

3.4. KAM distribution and GND density

3.4.1. KAM distribution

In EBSD measurements, KAM mapping analysis provides accurate quantification of the local plastic strains of different materials [25,53]. In the present study, high KAM values (> 1°) defined deformed grains whereas low KAM values (< 1°) defined recrystallised grains [54]. Fig.15 shows KAM maps and local misorientation angle distribution maps of the coarse-grained sample before and after compression and at different regions of the sample. In these maps, the blue, green, and red colors represent various levels of dislocation density or the degree of strain localisation, namely, from low to high. In Figs.17a_1 and a_2, both the top and middle regions of the non-deformed

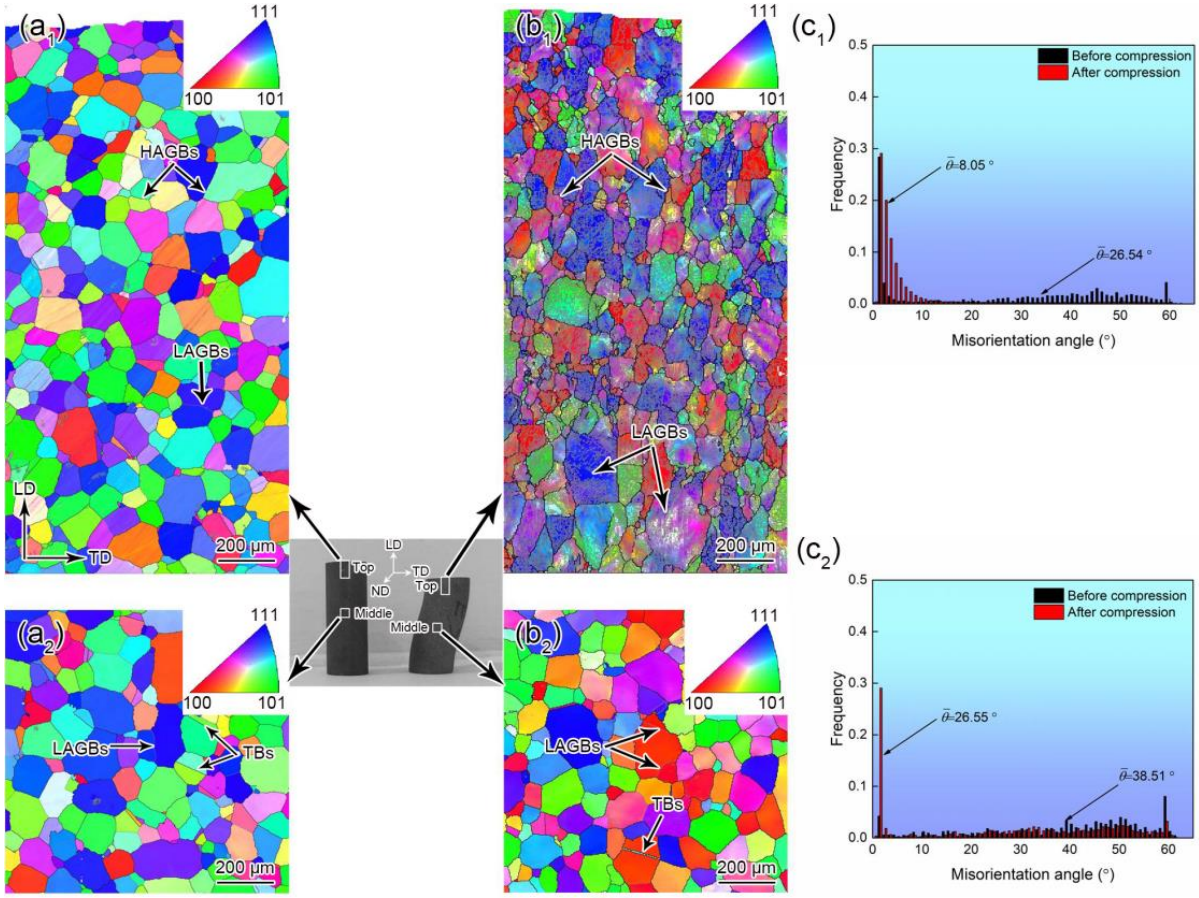

Fig.15 Microstructures of the fine-grained sample before and after compression in the top and middle regions: (a_1) and (a_2) are IOM maps before compression; (b_1) and (b_2) are IOM maps after compression; (a_1) and (b_1) are the top region and (a_2) and (b_2) are the middle region; (c_1) is the misorientation angle distribution map before and after compression in the top region; (c_2) is the misorientation angle distribution map before and after compression in the middle region.

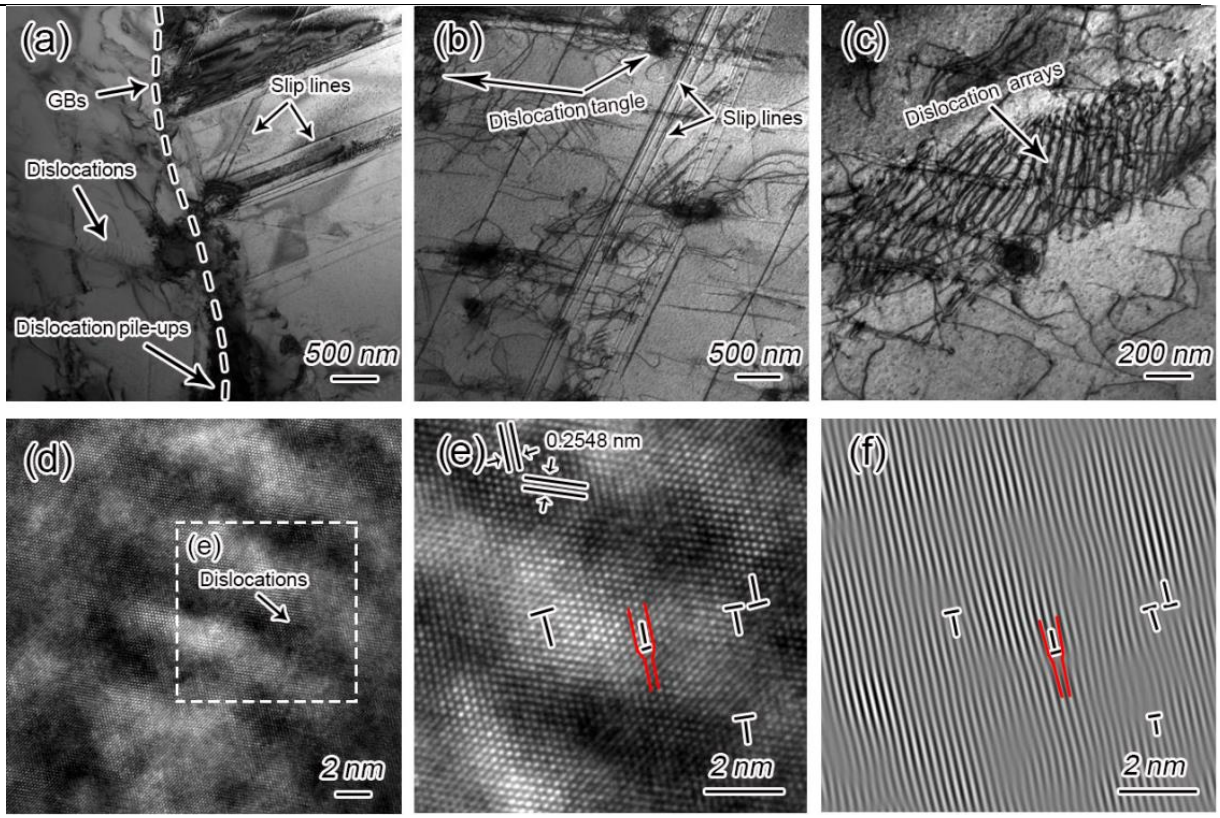

Fig.16 Typical deformed microstructure at room temperature in fine-grained Inconel 625 alloy: (a) low magnification TEM images wherein GBs impede dislocation motion and dislocation pile-ups at GBs; (b) low magnification TEM images wherein different dislocation configuration morphologies are observed; (d) HRTEM micrograph of dislocations; (e) HRTEM micrograph from the region outlined with a white rectangle in (d); (f) FFT image of (e) clearly showing dislocations locations. Edge dislocations are marked by black “T”s in (e and f).

coarse-grained sample exhibit uniform strain distribution both inside the grains and across the grain boundaries.

After compression deformation, the observed strain concentrations were both intragranular and at the GBs in the top region (Fig.17b_1), while the observed strain concentrations were at the GBs in the middle region (Fig.17b_2). Meanwhile, the degree of strain concentration or localisation in the top region is significantly higher than that in the middle region. The varying strain concentration indicates gradual decrease in the scale of compressive deformation, from the top to middle region. In other words, the top region is the high-strain region while the middle region is the low-strain region. In Fig.17c_1 and c_2, the KAM value is 1.93 ° in the top region, indicating that the microstructure is primarily comprised of deformed grains (Fig.17b_1). However, the KAM value is 0.43 ° in the middle region, indicating that the microstructure remained as the original recrystallised grains (Fig.15b_2).

Fig.18 shows KAM maps and local misorientation angle distribution maps before and after compression for the fine-grained sample. From Fig.18, the KAM distribution and local misorientation angle distribution of the fine-grained sample features are similar to the coarse-grained sample, indicating that the degree of deformation decreases gradually, from top region to middle region, in the fine-grained sample during compression. Meanwhile, the microstructure in the top region of the fine-grained sample after compression mainly consist of deformed grains, while the microstructure in the middle region of the fine-grained sample after compression is mainly original recrystallized grains.

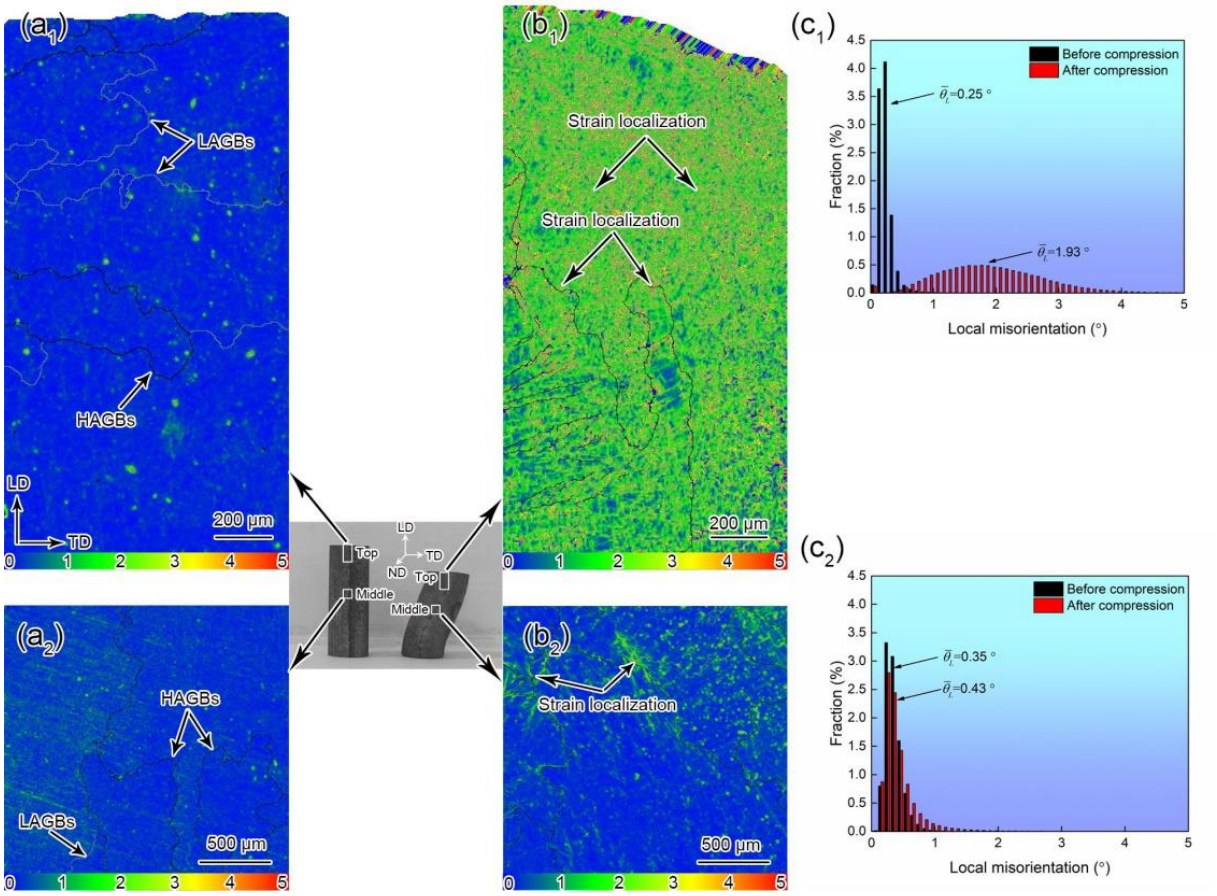

Fig.17 KAM maps and local misorientation angle distribution maps before and after compression for coarse-grained samples at different regions: (a_1) and (a_2) are KAM maps before compression; (b_1) and (b_2) are KAM maps after compression; (a_1) and (b_1) are the top region and (a_2) and (b_2) are the middle region; (c_1) is the local misorientation angle distribution map before and after compression in the top region; (c_2) is the local misorientation angle distribution map before and after compression in the middle region.

3.4.2. GND density

According to Gao et al. [55] and Kubin and Mortensen [56], the relationship between local intergranular misorientation (θ_L) and GND density (ρ^{GND}) is expressed as

$$\rho^{\mathrm{GND}} = \frac{2\theta_L}{\mu b} \quad (5)$$

where μ is the unit length of the point (100 nm) and b is the Burgers vector (0.253 nm for Inconel 625 alloy). The calculated ρ^{GND} values before and after the compression of coarse-grained and fine-grained Inconel 625 alloys are shown in Figs.19a and b, respectively. The most significant finding is that the deformed top regions of both the coarse-grained and the fine-grained samples showed much higher GND density than all other regions (by a factor of ten). This is the primary reason for the gradual decrease in the degree of deformation or strain localisation from the deformed top region to the deformed middle region. Meanwhile, the GND density in the deformed top region of the fine-grained sample is higher than that in the equivalent region of the coarse-grained sample while the GND densities in the middle regions are basically the same. This result is consistent with calculations from in-situ neutron diffraction (Fig.12).

Fig.20 shows the φ_2 = 0 ° and φ_2 = 45 ° sections of the orientation distribution function (ODF) of the top and middle regions of the coarse-grained sample before and after compressive deformation. The non-deformed top region shows a weak Rotated-Goss texture, {110}<110> (Fig.20a), while the deformed top region shows strong Brass-R textures, {111}<110> and

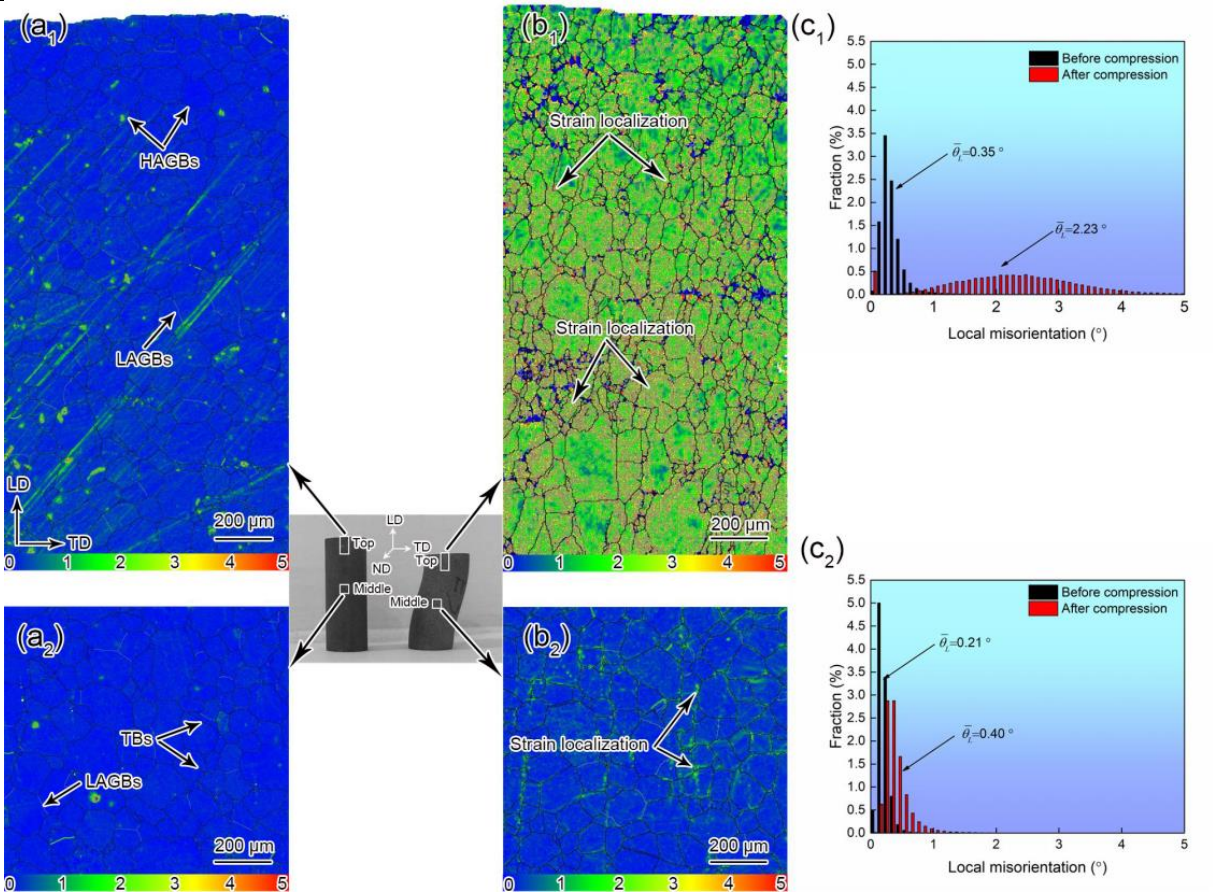

Fig.18 KAM maps and local misorientation angle distribution maps before and after compression for fine-grained samples at different regions: (a_1) and (a_2) are KAM maps before compression; (b_1) and (b_2) are KAM maps after compression; (a_1) and (b_1) are the top region and (a_2) and (b_2) are the middle region; (c_1) is the local misorientation angle distribution map before and after compression in the top region; (c_2) is the local misorientation angle distribution map before and after compression in the middle region.

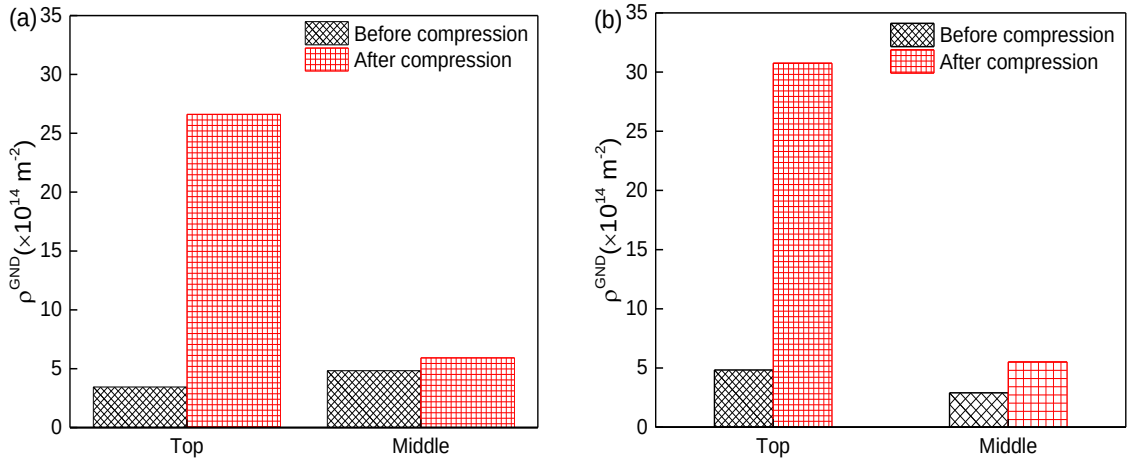

Fig.19 GND density in different regions before and after compression of the Inconel 625 alloy for the (a) coarse-grained and (b) fine-grained samples.

{111}<112>, as well as a weak Rotated-Goss texture, {110}<110> (Fig.20b). These results indicate the formation of strong Brass-R textures that is induced by compression deformation of the coarse-grained sample, which is attributed to dislocation slipping ({111}<110>) and deformation twinning ({111}<112>). The non-deformed middle region exhibited a weak Brass-R

texture, {111}<110> (Fig.20c), which transformed to the combined strong Twinned-Copper texture {552}<115> and Brass texture, {110}<112>, as well as, weak Goss texture, {110}<001>, after the deformation (Fig.20d). This transition of texture has been previously attributed to deformation twinning [57]. Compared to the top region, the middle region has a lower degree of deformation during compression deformation. Meanwhile, because Inconel 625 alloy has an FCC crystalline structure with low SFE, compression deformation is expected to be accompanied by the transformation of the initial Copper orientation, {112}<111>, to twinned-Copper orientation, {552}<115>, through twinning, which subsequently enables slipping motion of dislocations to reorient to Brass orientation, {110}<112>, through an intermediate Goss orientation, {110}<001> [58].

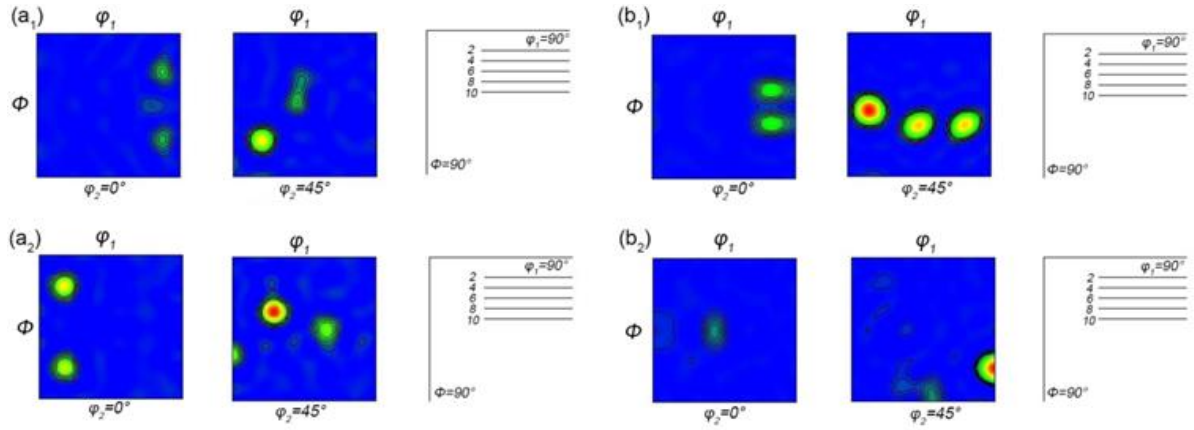

Fig.20 φ_2 = 0 ° and φ_2 = 45 ° sections of the ODF for the coarse-grained sample before and after deformation at different regions: (a) and (c) correspond to before deformation; (b) and (d) correspond to after deformation; (a) and (b) correspond to the top region; and (c) and (d) correspond to the middle region.

3.5. Texture evolution

Fig.21 shows the φ_2 = 0° and φ_2 = 45° sections of the ODF of the fine-grained samples at varying conditions. The non-deformed top region exhibited a mixture of strong Rotated-Goss texture, {110}<110> , weak Brass texture, {110}<112>, and Brass-R texture, {111}<110>, with an appearance by {111}<112> (Fig.21a). The deformed top region shows a mixture of a strong Rotated-Cube texture, {001}<110>, and weak Brass-R texture, {111}<110> and {112}<110> (Fig.21b). In the middle region, the weak Brass-R texture, {111}<110>, appears before deformation (Fig.21c), while the strong Goss texture, {110}<001>, weak Brass texture, {110}<112>, Rotated-Cube texture, {001}<110>, and Brass-R texture, {111}<110>, appears after deformation (Fig.21d). Compared to the top region, the middle region has a strong Goss texture, {110}<001>, and a weak Brass texture, {110}<112>, which is attributed to deformation twinning [58].

Compared to the fine-grained sample, the coarse-grained sample has stronger texture intensity during compression deformation, which is consistent with the texture variations previously analyzed by neutron diffraction peak intensity. Combined with texture analysis, it is again suggested that the coarse-grained sample is more conducive to the formation of deformation twins during compression.

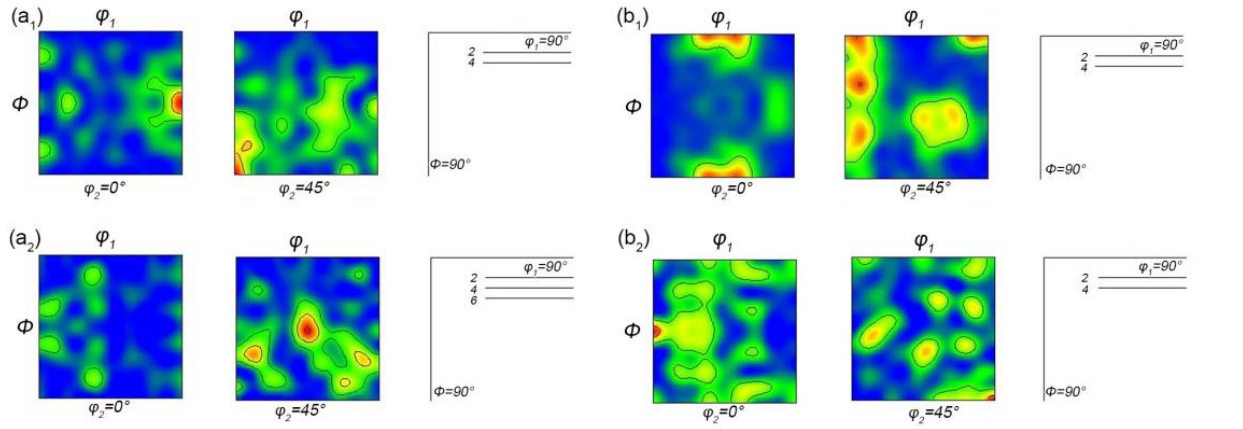

Fig.21 φ_2 = 0 ° and φ_2 = 45 ° sections of the ODF for the fine-grained sample before and after deformation at different regions: (a) and (c) correspond to before deformation; (b) and (d) correspond to after deformation; (a) and (b) correspond to the top region; and (c) and (d) correspond to the middle region.

4. Discussion

4.1. Stacking fault energy calculation

Stacking fault energy is defined as the energy per fault area by dissociating a perfect dislocation into two Shockley partial dislocations, which is often considered as a surface tension pulling the partials. Generally, two methods have been widely used to determine the value of SFE, including the TEM-based direct method and an indirect method using X-ray diffraction (XRD) [59, 60]. By measuring the spacing between two Shockley partial dislocations acquired by TEM imaging, the SFE can be calculated from the following [61]:

$$\gamma_{SF}=\frac{Gb_p^2}{8\pi\cdot w}\cdot\left(\frac{2-\upsilon}{1-\upsilon}\right)\cdot\left(1-\frac{2\upsilon\cos 2\Phi}{2-\upsilon}\right) \quad (6)$$

where γ_{SF} is the SFE, G is the shear modulus, v is Poisson's ration, b_p is the Burgers vector of partial dislocations, w is the measured SF width, and Φ corresponds to the angle between the dislocation line and the Burgers vector. Fig.22 shows a typical HRTEM image of an extended dislocation configuration in the coarse-grained sample, which clearly shows a SF existing between two Shockley partial dislocations. Thus, the corresponding SFE of the coarse-grained Inconel 625 alloy can be estimated according to Eq. (6). For the calculation, G is 79 GPa, v is 0.308, b_p is 0.147 nm, w is the SF width measured from our TEM images, and Φ is 0 °. All the SF widths measured by HRTEM are recorded in Table 3. By substituting the corresponding values, the average SFE of the γ matrix in coarse-grained Inconel 625 alloy is calculated to be 52.65 ± 6.75 mJ/m^2.

Table 3 Parameters used for calculation and stacking fault energy in coarse-grained Inconel 625 alloy.

Alloy	Stacking fault width (nm)				Average γ_{SF} (mJ/m^2)
	1	2	3	4	
Inconel 625	2.42	1.98	1.98	1.76	52.65 ± 6.75

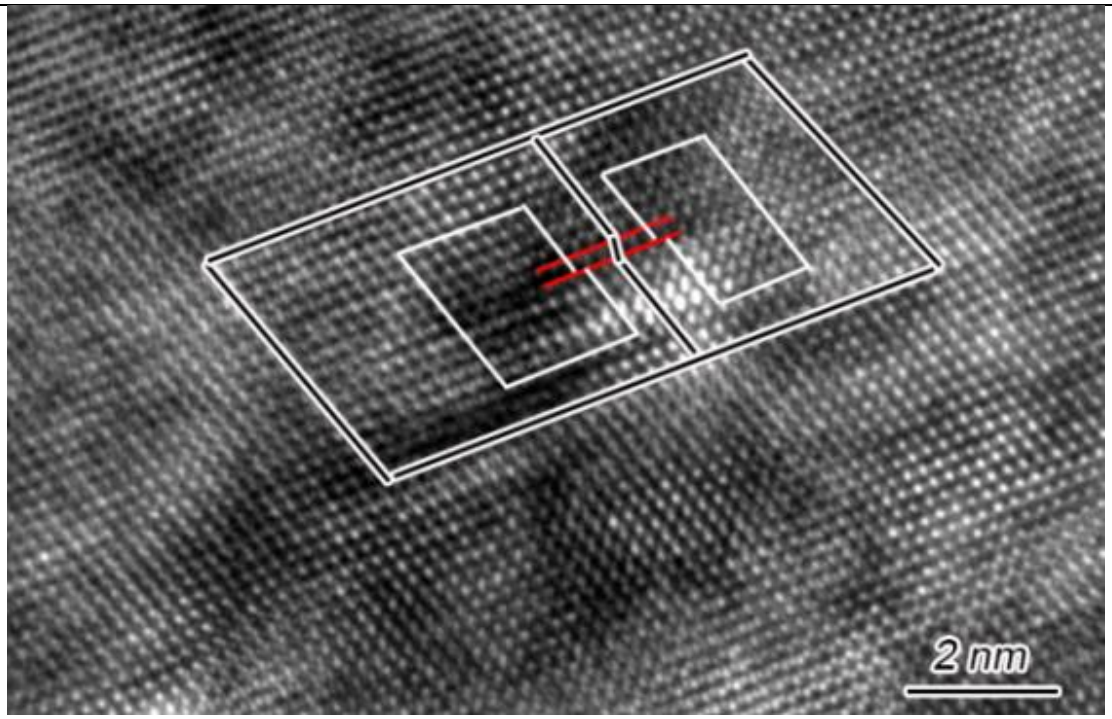

Fig.22 A typical HRTEM image of an extended dislocation configuration in the coarse-grained sample.

4.2. The effect of grain size on deformation mechanisms

Generally, the deformation mechanisms in FCC metals and alloys during plastic deformation are associated with their SFE and deformation conditions, such as strain, strain rates, and temperature [62]. FCC metals and alloys with high SFEs likely deform by dislocation slip during room temperature plastic deformation [63]. On the other hand, FCC metals and alloys with intermediate SFEs deform by twinning at high-strain rates and/or at low deformation temperatures by dislocation slipping at low-strain rates and/or at high deformation temperatures [64]. In addition, the deformation mechanisms in FCC metals and alloys were strongly dependent on grain size at room temperature. In particular, increasing the average grain size results in lower twinning nucleation stress for a given metal and alloy [65, 66]. Early studies [67, 68] found that the relationship between grain size and critical resolved shear stress for twinning obeys the Hall-Petch-type relation,

$$\tau_{tw} = \frac{\gamma_{SF}}{b} + \frac{K_{tw}^{H-P}}{\sqrt{D}} \quad (7)$$

where γ_{SF} is the SFE, b is the Burgers vector, K_{tw}^{H-P} is the Hall-Petch constant for twinning, and D is the grain size. These stresses were calculated according to,

$$\sigma_{tw} = M\tau_{tw} = M(\frac{\gamma_{SF}}{b} + \frac{K_{tw}^{H-P}}{\sqrt{D}}) \quad (8)$$

where M = 3 is the Taylor factor. In present study, K_{tw}^{H-P} was unknown and K_{slip}^{H-P} equal to 750 MPa $\mu m^{1/2}$, for pure Ni and a range of superalloys [69], was used instead.

Based on the above studies, we know that the Inconel 625 alloy, as an FCC metal with low-to-medium SFE, is deformed by the combined mechanisms of dislocation slipping in the {111}<110> system and twinning in the {111}<112>. However, the activation of twinning was dependent on the initial grain size of the Inconel 625 alloy. The contribution of SFE and grain size to the twinning stresses of the Inconel 625 alloy can be analysed separately using Eq. (8). The results are shown

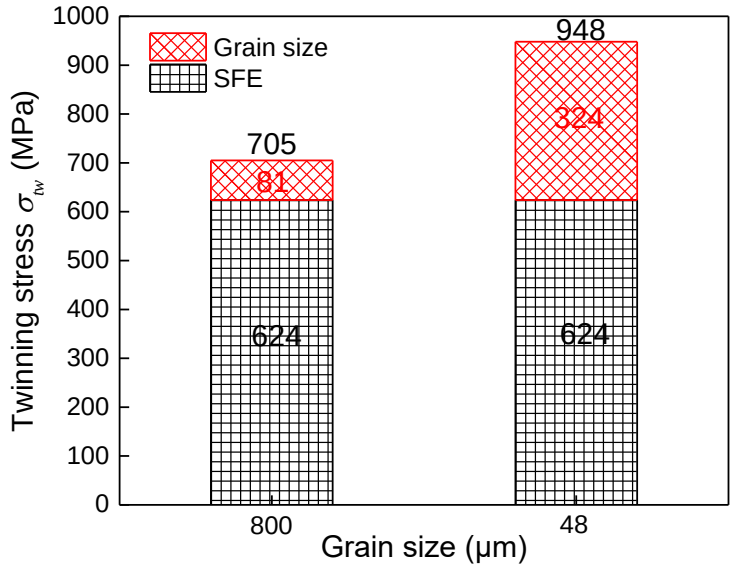

Fig.23 Twinning stress contribution from SFE and grain size in coarse-grained (D = 800 μm) and fine-grained (D = 48 μm) samples.

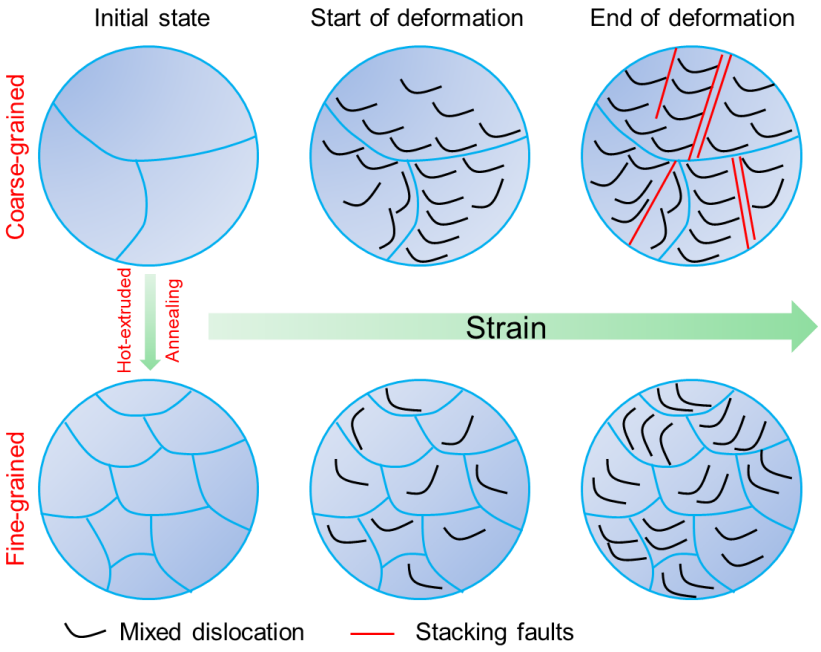

Fig.24 The deformation mechanisms of the coarse-grained and fine-grained samples at room temperature.

in Fig. 23. It can be seen that in both the coarse-grained and the fine-grained Inconel 625 alloys the contributions of SFE to twinning stress are larger than that of grain size.

Meanwhile, the twinning stress required for the coarse-grained Inconel 625 alloy during compression deformation is lower than that for the fine-grained Inconel 625 alloy. In addition, the contribution of grain size to the twinning stress of Inconel 625 alloy increases with decreasing grain size. Fig.24 summarises the deformation mechanism of the coarse-grained and fine-grained samples at room temperature. For the coarse-grained sample, plastic deformation is composed of complicated interactions among mixed dislocations (edge and screw dislocations) and stacking faults. For the fine-grained sample, multiplication and motion of mixed dislocations (edge and screw dislocations) is the dominant mechanism. Thus, the deformation mechanism of the coarse-

grained Inconel 625 alloy is mainly dislocation slipping that is accompanied by the formation of SFs to accommodate the deformation, while the deformation mechanism of the fine-grained Inconel 625 alloy is only dislocation slip. The above results indicated that the coarse-grained alloy was more conducive to the formation of SFs or deformation twins under the same applied stress.

In addition, for an FCC alloy with a specific grain size and SFE, grain orientation also has a significant influence on the deformation mechanism [21-22]. Earlier studies found that the influence of grain orientation on deformation twinning is commonly explained in terms of Schmid's law for slip twin dislocations [70, 71]:

$$\tau_{tw} = \sigma \cdot m \quad (9)$$

where m is the Schmid factor and σ is the macroscopic stress. Eq. (9) can be used to calculate the particular macroscopic stress that determines whether the grain orientations do or do not favor twinning deformation. Fig.25 shows the Schmid factor of the coarse-grained and fine-grained samples under different strain regions. It is clearly seen that the Schmid factor (m) in the low-strain region is lower than that in the high-strain region, indicating that it is favorable to twinning at a particular macroscopic stress. In the present study, the ODF analysis of the coarse-grained and fine-grained samples verified that the Brass orientation, {110}<112>, in the low-strain region was formed by the volume effect of deformation twinning (Figs.20d and 21d), but no Brass orientation was observed in the high-strain region. Thus, the effect of grain orientation on deformation mechanism is that the grain orientation has a strong influence on deformation twinning in the low-strain region, whereas the effect decreased significantly in the high-strain region.

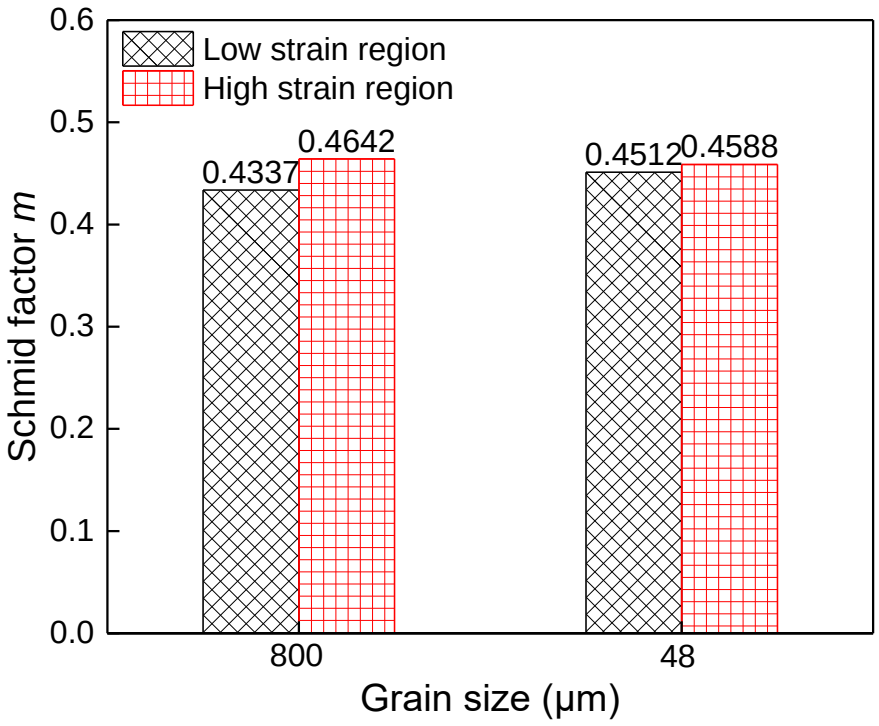

Fig.25 Schmid factor (m) of coarse-grained and fine-grained samples in different strain regions.

5. Conclusions

In this work, the effects of grain size on the elastic-plastic deformation behaviour and twinning behaviour of Inconel 625 alloy during compression deformation were investigated by in-situ neutron diffraction, EBSD and TEM. The following conclusions were drawn:

1) The Inconel 625 alloy showed strong crystal elastic and plastic anisotropy. The fine-grained alloy showed higher elastic modulus, E_{hkl}, than coarse-grained alloy for all analszed crystalline planes. Meanwhile, the (200) peak in the coarse-grained alloy appeared until the strain was more than ~−10.8 %, which was attributed to grain rotation. In addition, grain refinement not only improved both deformation compatibility and deformation homogeneity, but also enhanced the compression yield strength.
2) The deformed coarse-grained alloy showed a large number of multiple-slip lines, dislocations, and SFs with a SFE of 52 ± 6.75 mJ/m^2. The resultant microstructure was found to have a stronger Copper orientation, {112}<111>, as a result of dislocation slipping, while elongated deformed grains had a strong Brass orientation, {110}<112>, attributed to deformation twinning.
3) The deformed fine-grained alloy showed a large number of slip lines, dislocations, and dislocation pile-ups at grain boundaries, but no SFs. Furthermore, its dislocation density was higher than the coarse-grained alloy under the same applied stress.
4) The deformation mechanism of Inconel 625 alloy was strongly influenced by grain size. The coarse-grained alloy was more conducive to the formation of SFs or deformation twins owing to the decreased twinning stress.
5) Finally, grain orientation also has a significant influence on the deformation mechanisms during plastic deformation. It favours twinning in the low-strain region, compared to the high-strain region, at a particular macroscopic stress.

Credit authorship contribution statement

Yubi Gao: Writing-Original draft preparation, Writing-Reviewing. **Yutian Ding** and **Hongbiao Dong**: Conceptualization, Methodology, Supervision. **Haifeng Li** and **Quanshun Luo**: Visualization, Validation. **Ruiyao Zhang** and **Jun Li**: Investigation, Data Curation, Editing.

Declaration of competing interest

The authors declare that they have no known competing financial interests or personal relationships that could have appeared to influence the work reported in this paper.

Acknowledgements

This work was financially supported by the National Key Research and Development Program of China (Grant No.2017YFA07007003) and the National Natural Science Foundation of China (Grant No.51661019), the program for Major Projects of Science and Technology in Gansu Province (Grant No.145RTSA004), and Hongliu first-class discipline construction plan of Lanzhou University of Technology, and Incubation program of Excellent Doctoral Dissertation-Lanzhou University of Technology, and Lanzhou University of Technology Excellent Students Studying Abroad Learning Exchange Fund and State Key Laboratory of Cooperation and Exchange Fund. Tung-Lik Lee at ISIS provided invaluable assistance in performing the neutron diffraction experiments.

References

[1] Chakravartty JK, Singh JB, Sundararaman M. Microstructural and mechanical properties of service exposed alloy 625 ammonia cracker tube removed after 100 000 h. Energy Mater 2013; 28: 702-710.
[2] Shankar V, Rao KBS, Mannan SL. Microstructure and mechanical properties of Inconel 625 superalloy. J Nucl Mater 2001; 288: 222-232.
[3] Singh JB, Verma A, Jaiswal DM, Kumar N, Patel RD, Chakravartty JK. Rejuvenation of service exposed ammonia cracker tubes of cast alloy 625 and their re-use. Mater Sci Eng A 2015; 44: 254-267.
[4] Kumar N, Parameswaran P, Kumar N, Sandhya R, Mathew MD. Influence of re-solutionising treatment on the cyclic deformation behaviour of a service-exposed Inconel 625 superalloy. Mater High Temper 2014; 29: 49-53.
[5] Mathew MD, Rao KBS, Mannan SL. Creep properties of service-exposed alloy 625 after re-solution annealing treatment. Mater Sci Eng A 2004; 372: 327-333.
[6] Sundararaman M, Kumar L, Prasad GE, Mukhopadhyay P, Banerjee S. Precipitation of an intermetallic phase with Pt2Mo-type structure in alloy 625. Metall Mater Trans A 1999; 30: 41-52.
[7] Li XY, Lu K. Playing with defects in metals. Nat Mater, 2017; 16: 700–701.
[8] Yang L, Li XY, Lu K. Making materials plain: concept, principle and applications. Acta Metall Sin 2017; 53: 1413–1417.
[9] Li XY, Lu K. Improving sustainability with simpler alloys. Science 2019; 364: 733–734.
[10] Lu K, Lu L, Suresh S. Strengthening materials by engineering coherent internal boundaries at the nanoscale. Science, 2009; 324: 349-352.
[11] Wang J, Zhang XH. Twinning effects on strength and plasticity of metallic materials. MRS Bullentin 2016; 40: 274-281.
[12] Wang ZJ, Li QJ, Li Y, Huang LC, Lu L, Dao M, et al. Sliding of coherent twin boundaries. Nat Commun, 2017; 8: 1108–1115.
[13] Lu L, Shen YF, Chen XH, Qian LH, Lu K. Ultrahigh strength and high electrical conductivity in copper. Science, 2004; 304: 422-426.
[14] Lu L, Chen X, Huang X, Lu K. Revealing the maximum strength in nanotwinned copper. Science, 2009; 323: 607-610.
[15] Lu K. Stabilizing nanostructures in metals using grain and twin boundary architectures. Nat Rev Mater 2016; 1: 16019.
[16] Yuan Y, Gu YF, Cui CY, Osada T, Yokokawa T, Harada H. A novel strategy for the design of advanced engineering alloys—strengthening turbine disk superalloys via twinning structures. Adv Eng Mater 2011; 13: 296–300.
[17] Yuan Y, Gu YF, Osada T, Zhong ZH, Yokokawa T, Harada H. A new method to strengthen turbine disc superalloys at service temperatures. Scripta Mater 2012; 66: 884–889.
[18] He JH, Lavernia EJ. Development of nanocrystalline structure during cryomilling of Inconel 625. J Mater Res 2001; 16: 2724-2732.
[19] Tao NR, Zhang HW, Lu J, Lu K. Development of nanostructures in metallic materials with low stacking fault energies during surface mechanical attrition treatment (SMAT). Mater Trans 2003; 44: 1919-1925.
[20] El-Danaf E, Kalidindi RS, Doherty RD. Influence of grain size and stacking-fault energy on deformation twinning in fcc metals. Metall Mater Trans A 1999; 30: 1223-1233.
[21] Han WZ, Zhang ZF, Wu SD, Li SX. Combined effects of crystallographic orientation, stacking

fault energy and grain size on deformation twinning in fcc crystals. Philos Mag 2008; 88: 3011-3029.
[22] Yang P, Xie Q, Meng L, Ding H, Tang Z. Dependence of deformation twinning on grain orientation in a high manganese steel. Scripta Mater 2006; 55: 629-631.
[23] Santisteban JR, Daymond MR, James JA, Edwards L. ENGIN-X: A third-generation neutron strain scanner. J Appl Crystallogr 2006; 39: 812–825
[24] Jiang J, Britton TB, Wilkinson AJ. Measurement of geometrically necessary dislocation density with high resolution electron backscatter diffraction: effects of detector binning and step size. Ultramicroscopy 2013; 125: 1–9.
[25] Wright SI, Nowell MM, Field DP. A review of strain analysis using electron backscatter diffraction. Microsc Microanal 2011; 17: 316–329.
[26] Wang H, Clausen B, Capolungo L, Beyerlein IJ, Wang J, Tomé CN. Stress and strain relaxation in magnesium AZ31 rolled plate: In-situ neutron measurement and elastic viscoplastic polycrystal modeling. Int J Plasticity 2016; 79: 275-292.
[27] Hansen N. Hall–Petch relation and boundary strengthening. Scripta Mater 2004; 51: 801-806.
[28] Song WX. Metallic. Beijing: Metallurgical Industry Press 2014; 141-142.
[29] Harjo S, Tomota Y, Lukáš P, Neov D, Vrána M, Mikula P, et al. In situ neutron diffraction study of α–γ Fe–Cr–Ni alloys under tensile deformation. Acta Mater 2001; 49: 2471-2479.
[30] Holden T M, Holt R A, Clarke A P. Intergranular strains in Inconel-600 and the impact on interpreting stress fields in bent steam-generator tubing. Mater Sci Eng A 1998; 246: 180–198.
[31] Holden T M, Clarke A P, Holt R A. Neutron diffraction measurements of intergranular strains in MONEL-400. Metall Mater Trans A 1997; 28: 2565-2576.
[32] Wang Z, Stoica AD, Ma D, Beese AM. Diffraction and single-crystal elastic constants of Inconel 625 at room and elevated temperatures determined by neutron diffraction. Mater Sci Eng A 2016; 674: 406-412.
[33] Cai B, Liu B, Kabra S, Wang YQ, Yan K. Deformation mechanisms of Mo alloyed FeCoCrNi high entropy alloy: In situ neutron diffraction. Acta Mater 2017; 127: 471-480.
[34] Clausen B, Lorentzen T, Bourke MAM, Daymond M R. Lattice strain evolution during uniaxial tensile loading of stainless steel. Mater Sci Eng A 1999; 259: 17–24.
[35] Woo W, Huang EW, Yeh JW, Choo H, Lee C, Tu SY. In-situ neutron diffraction studies on high-temperature deformation behaviour in a CoCrFeMnNi high entropy alloy. Intermetallics, 2015; 62: 1-6.
[36] Barabash RI, Ice GE, Walker FJ. Quantitative microdiffraction from deformed crystals with unpaired dislocations and dislocation walls. J Appl Phys 2003; 93: 1457-1464.
[37] Ungár T. Microstructural parameters from X-ray diffraction peak broadening. Scripta Mater 2004; 51: 777-781.
[38] Ungar T, Gubicza J, Ribarik G, Borbely A. Crystallite size distribution and dislocation structure determined by diffraction profile analysis: principles and practical application to cubic and hexagonal crystals. J Appl Crystallogr 2001; 34: 298-310.
[39] Francis EM, Grant BMB, Fonseca JQD, Phillips PJ, Mills MJ, Daymond MR, et al. High-temperature deformation mechanisms in a polycrystalline nickel-base superalloy studied by neutron diffraction and electron microscopy. Acta Mater 2014; 74: 18-29.
[40] Borbély A, Driver J H, Ungár T. An X-ray method for the determination of stored energies in texture components of deformed metals; Application to cold worked ultra high purity iron. Acta Mater 2000, 31(8): 2005-2016.
[41] Wang X L, Wang Y D, Stoica A D, Horton D J, Tian H, Liaw P K, Choo H, Richardson J W,

Maxey E. Inter- and intragranular stresses in cyclically-deformed 316 stainless steel. Mater Sci Eng A, 2005, 399(1/2): 114-119.
[42] Wu Y, Liu W H, Wang X L, Ma D, Stoica A D, Nieh T G, He Z B, Lu Z P. In-situ neutron diffraction study of deformation behaviour of a multi-component high-entropy alloy. Appl Phys Lett 2014, 104(5):633-93.
[43] Liang XZ, Dodge MF, Kabra S, Kelleher JF, Lee TL, Dong HB. Effect of hydrogen charging on dislocation multiplication in pre-strained super duplex stainless steel. Scripta Mater 2018; 143: 20-24.
[44] Taylor GI. The mechanism of plastic deformation of crystals. P Roy Soc A 1934; 145: 362–387.
[45] Margulies L, Winther G, Poulsen HF. In situ measurement of grain rotation during deformation of polycrystals. Science 2001; 291: 2392-2394.
[46] Madhavan R, Ray RK, Suwas S. Texture transition in cold-rolled nickel-40 wt.% cobalt alloy. Acta Mater 2014; 74: 151-164.
[47] Li B L, Godfrey A, Meng QC, Liu Q, Hansen N. Microstructural evolution of IF-steel during cold rolling. Acta Mater 2004; 52:1069–1081.
[48] Tao NR, Wu XL, Sui ML, Lu J, Lu K. Grain refinement at the nanoscale via mechanical twinning and dislocation interaction in a nickel-based alloy. J Mater Res 2004; 19: 1623-1629.
[49] Xu YJ, Qi DQ, DuK, Cui CY, Ye HQ. Stacking fault effects on dynamic strain aging in a Ni-Co-based superalloy. Scripta Mater 2014; 87: 37-40.
[50] Bailey JE, Hirsch PB. The recrystallization process in some polycrystalline metals. P Roy Soc A 1962; 267: 11–30.
[51] Fullman RL, Fisher JC. Formation of annealing twins during grain growth. J Appl Phys 1951; 22: 1350–1355.
[52] Randle V. ‘Special’ boundaries and grain boundary plane engineering. Scripta Mater 2006; 54: 1011–1015.
[53] Hou J, Peng QJ, Lu ZP, Shoji T, Wang JQ, Han EH, et al. Effects of cold working degrees on grain boundary characters and strain concentration at grain boundaries in Alloy 600. Corros Sci 2011; 53: 1137-1142.
[54] Satheesh KSS, Raghu T, Bhattacharjee PP, Rao GA. Work hardening characteristics and microstructural evolution during hot deformation of a nickel alloy at moderate strain rates. J Alloy Comp 2017; 709: 394–409.
[55] Gao H, Huang Y, Nix WD, Hutchinson JW. Mechanism-based strain gradient plasticity— I. Theory. J Mech Phys Solids 1999; 47: 1239–1263.
[56] Kubin LP, Mortensen A. Geometrically necessary dislocations and strain-gradient plasticity: a few critical issues. Scripta Mater, 2003; 48: 119–125.
[57] Heye W, Wassermann G. Mechanical twinning in cold-rolled silver single crystals. Phys Status Solidi 1966; 18: 107-111.
[58] Heye W, Wasserman G. The formation of the rolling textures in FCC metals by slip and twinning. Scripta Metall 1968; 2: 205-207.
[59] Reed RP, Schramm RE. Relationship between stacking-fault energy and x-ray measurements of stacking-fault probability and microstrain. J Appl Phys 1974; 45: 4705-4711.
[60] Aerts E, Delavignette P, Siems R, Amelinckx S. Stacking fault energy in silicon. J Appl Phys 1962; 33: 3078-3080.
[61] Murr LE. Stacking-fualt anomalies and the measurement of stacking-fault free energy in FCC thin films. Thin Solid Films 1969; 4: 389-412.
[62] Dillamore IL. The stacking fault energy dependence of the mechanisms of deformation in Fcc

metals. Metall Trans 1970; 1: 2463-2470.
[63] Rohatgi A, Gray VGT. The influence of stacking fault energy on the mechanical behaviour of Cu and Cu-Al alloys: Deformation twinning, work hardening, and dynamic recovery. Metall Mater Trans A 2001; 32: 135-145.
[64] Sarma VS, Wang J, Jian WW, Kauffmann A, Conrad H, Freudenberger J, Zhu YT. Role of stacking fault energy in strengthening due to cryo-deformation of FCC metals. Mater Sci Eng A 2010; 527: 7624-7630.
[65] Gutierrez-Urrutia I, Raabe D. Grain size effect on strain hardening in twinning-induced plasticity steels. Scripta Mater 2012; 66: 992-996.
[66] Rahman KM, Vorontsov VA, Dye D. The effect of grain size on the twin initiation stress in a TWIP steel. Acta Mater 2015, 89: 247-257.
[67] Meyers MA, Vohringer O, Lubarda VA. The onset of twinning in metals: a constitutive description. Acta Mater 2001; 49: 4025-4039.
[68] Gutierrez-Urrutia I, Zaefferer S, Raabe D. The effect of grain size and grain orientation on deformation twinning in a Fe-22 wt.% Mn-0.6 wt.% C TWIP steel. Mater Sci EngA, 2010; 527: 3552-3560.
[69] Kozar RW, Suzuki A, Milligan WW, Schirra JJ, Savage MF, Pollock TM. Strengthening mechanisms in polycrystalline multimodal Nickel-base superalloys. Metall Mater Trans A 2009; 40: 1588–1603.
[70] Bracke L, Kestens L, Penning J. Direct observation of the twinning mechanism in an austenitic Fe-Mn-C steel. Scripta Mater 2009; 61: 220-222.
[71] Karaman I, Sehitoglu H, Gall K, Maier HJ. Deformation of single crystal Hadfield steel by twinning and slip. Acta Mater 2015; 48: 1345-1359.